Monthly Notices
of the
ROYAL ASTRONOMICAL SOCIETY

MNRAS **479,** 2564–2587 (2018)
Advance Access publication 2018 June 14

doi:10.1093/mnras/sty1563

Lyman-α emitters gone missing: the different evolution of the bright and faint populations

Lewis H. Weinberger,[1]★ Girish Kulkarni,[1] Martin G. Haehnelt,[1] Tirthankar Roy Choudhury[2] and Ewald Puchwein[1]

[1]*Institute of Astronomy and Kavli Institute for Cosmology, University of Cambridge, Madingley Road, Cambridge CB3 0HA, UK*
[2]*National Centre for Radio Astrophysics, Tata Institute of Fundamental Research, Pune 411007, India*

Accepted 2018 June 8. Received 2018 June 8; in original form 2018 March 8

ABSTRACT

We model the transmission of the Lyman-α line through the circum- and intergalactic media around dark matter haloes expected to host Lyman-α emitters (LAEs) at $z \geqslant 5.7$, using the high-dynamic-range Sherwood simulations. We find very different circumgalactic medium (CGM) environments around more massive haloes ($\sim 10^{11} \mathrm{M}_{\odot}$) compared to less massive haloes ($\sim 10^{9} \mathrm{M}_{\odot}$) at these redshifts, which can contribute to a different evolution of the Ly α transmission from LAEs within these haloes. Additionally, we confirm that part of the differential evolution could result from bright LAEs being more likely to reside in larger ionized regions. We conclude that a combination of the CGM environment and the intergalactic medium (IGM) ionization structure is likely to be responsible for the differential evolution of the bright and faint ends of the LAE luminosity function at $z \geqslant 6$. More generally, we confirm the suggestion that the self-shielded neutral gas in the outskirts of the host halo can strongly attenuate the Ly α emission from high redshift galaxies. We find that this has a stronger effect on the more massive haloes hosting brighter LAEs. The faint-end of the LAE luminosity function is thus a more reliable probe of the average ionization state of the IGM. Comparing our model for LAEs with a range of observational data, we find that the favoured reionization histories are our previously advocated 'Late' and 'Very Late' reionization histories, in which reionization finishes rather rapidly at around $z \simeq 6$.

Key words: galaxies: high-redshift – galaxies: evolution - dark ages, reionization, first stars – intergalactic medium – cosmology: theory.

1 INTRODUCTION

Observations such as the Lyman-α (Ly α) forest in quasar spectra (Fan et al. 2006; Becker et al. 2015; McGreer, Mesinger & D'Odorico 2015) and the Thomson optical depth to the Cosmic Microwave Background (CMB) (Planck Collaboration XLVII 2016) suggest that the neutral hydrogen fraction of the intergalactic medium (IGM) increases between redshifts of $z \sim 6$ and $z \sim 10$ during the Epoch of Reionization (EoR). This final phase transition of the Universe is, however, not yet completely understood; in particular, there is still some debate about the contribution of different sources responsible for the reionization of hydrogen (Duncan & Conselice 2015). To make progress requires further improved knowledge of the luminosity functions and the escape fractions of ionizing photons for possible candidates for which the faint end is particularly challenging at high redshifts (Richards et al. 2006; Bouwens et al. 2015; Yue, Ferrara & Xu 2016; McGreer et al. 2018). Firmer constraints on the exact redshifts at which the reionization process began and ended are also challenging to obtain, due to the still rather scarce data and the model dependence of the constraints obtained from observations (for a review of IGM models, see Choudhury 2009; Meiksin 2009, and references therein). Greig & Mesinger (2017), for example, used a Bayesian framework to combine a selection of observational results but noted, as other authors have, that there are degeneracies between the EoR parameters that cannot yet be broken by current observations.

One notable observation made in recent years is the dramatic decline in the space density of Ly α-emitting galaxies (LAEs) beyond $z > 6$ (Kashikawa et al. 2006; Hu et al. 2010; Ouchi et al. 2010; Konno et al. 2014), compared to continuum-selected galaxies (Stark, Ellis & Ouchi 2011; Schenker et al. 2012; Pentericci et al. 2014; Bouwens et al. 2015). Note that at lower redshifts ($3 \lesssim z \lesssim 5$, after hydrogen reionization), however, the LAE luminosity function shows little evolution (Hu, Cowie & McMahon 1998; Ouchi et al. 2008). With an increasingly neutral fraction of hydrogen beyond z

★ E-mail: lewis.weinberger@ast.cam.ac.uk

~ 6, we expect more of the Ly α emission to be absorbed and scattered by the IGM and hence a reduction in observed flux compared to the continuum. This has been used to obtain model-dependent constraints on the evolution of the neutral hydrogen fraction. For example, Ota et al. (2017) used the model of Santos (2004) to convert an Ly α transmission ratio into a fraction $x_{\rm HI}^{z=7} \gtrsim 0.3-0.4$.

There have been a number of analytic and numerical models developed to explain the apparent rapid decline of Ly α emission from galaxies; for example taking into account the role of dust and reionization (Dayal et al. 2009), of self-shielded absorbers (Bolton & Haehnelt 2013; Choudhury et al. 2015), the infall of the CGM onto the host haloes (Sadoun, Zheng & Miralda-Escudé 2017), or ruling out the role of IGM attenuation as a sole factor (Mesinger et al. 2015).

One of the difficulties in explaining this decline is the dependence of the IGM transmission on the Ly α emission line profile of the galaxy, which is complicated by the Ly α radiative transfer out of the galaxy's interstellar medium (ISM). It has been found empirically that the peak of the emission profile is often offset redwards from the Ly α frequency (Erb et al. 2010). Studies at lower redshifts have found correlations between this offset and emission properties such as line magnitude or equivalent width (Yang et al. 2016). For high redshifts, the usual reference lines for determining this offset (such as [O III] or Hα) are not observable with ground-based telescopes. This leaves either using scaling relationships from low redshift observations (Erb et al. 2014) or, if available, using detections of lines such as C III]λ1909 (Stark et al. 2015).

Theoretical modelling of the Ly α emission profile is made difficult by the resonant nature of the line, resulting in emission profiles that are strongly affected by the ISM (Zheng et al. 2010). Use of Monte Carlo radiative transfer codes (Orsi, Lacey & Baugh 2012; Gronke & Dijkstra 2016) and analytic methods (Dijkstra, Haiman & Spaans 2006) has led to simple parametrized models of the emission profile such as the shell model (Gronke, Bull & Dijkstra 2015), but see, for example, Barnes et al. (2011) for more realistic models. The sensitivity of the emission profiles to the physical and dynamical state of hydrogen in and around galaxies makes isolating the intrinsic galaxy evolution from the IGM evolution very difficult.

Recent surveys probing beyond $z = 7$ have found a further complication: some observers have measured a luminosity dependence for the attenuation of quantities such as the luminosity function and the LAE fraction (Curtis-Lake et al. 2012; Konno et al. 2014; Matthee et al. 2015; Santos, Sobral & Matthee 2016; Zheng et al. 2017). Faint ($M_{\rm UV} > -20.25$) LAEs are observed to decline in number in a similar manner beyond $z = 7$ as was seen for $z = 5$–6, and this has been used to extrapolate reionization histories. For bright ($M_{\rm UV} < -20.25$) LAEs, however, a much slower evolution has been observed. This can be most clearly seen in the luminosity functions of Zheng et al. (2017) and Ota et al. (2017), as well as the estimated LAE fraction in Stark et al. (2017). One suggested explanation (Zitrin et al. 2015) for this much weaker decline in the number of bright LAEs is that such galaxies sit in (and contribute ionizing photons to) larger ionized bubbles and hence are preferentially more visible than fainter galaxies.

There has been some recent theoretical work using simulations to explore the causes of these observations. Mason et al. (2018) explored the effect of a mass-dependent intrinsic velocity offset in the emission profile of LAEs, finding that larger velocity offsets can increase the visibility of bright LAEs. Inoue et al. (2018) explored the effect of a mass-dependent optical depth in the host halo and found that such a dependence was required to explain observations. In this work, we will further explore such effects, as well as the different roles the larger IGM environment can play around bright and faint LAEs.

There has also been some discussion in the literature of the effects of different selection techniques used for characterizing LAEs (Stark et al. 2010), which can be divided into two categories: (i) (broadband) ultraviolet (UV) selection with spectroscopic follow-up (as in Stark et al. 2011, for example), and (ii) direct (narrow-band) Ly α selection (as in Konno et al. 2014, for example). We note that observed LAE fractions are found via the former method, whilst most LAE luminosity functions are presented for populations found using the latter technique. In both cases, the selection effects (such as active galactic nuclei (AGN) contamination) may play an important role in the inferred properties of high redshift LAEs. Importantly for our modelling, the selection technique will affect the mapping between galaxy mass and Ly α (or UV) luminosity. We discuss this further in Section 6.3.

In this paper, we use a semi-analytic treatment of reionization, combined with the high-dynamic-range Sherwood simulations (Bolton et al. 2017), to explore the effect of the IGM environment on the luminosity-dependent LAE evolution. In Section 2, we outline our simulation set-up and calibration, which are based on Choudhury et al. (2015). Section 3 describes the framework we employ for calculating the transmission of Ly α radiation through the IGM. We establish models for reionization and for the LAEs in Section 4. We then present our results for these different models in Section 5. In Section 6, we discuss these results in comparison to other work, and finally draw conclusions in Section 7.

2 SIMULATION METHOD

In order to investigate the role of the IGM on LAE observations, we use cosmological hydrodynamical simulations with a semi-analytic treatment of reionization. There are two components to our numerical modelling: (i) a simulation of the (partially reionized) IGM, which includes the spatial distribution of neutral hydrogen, the peculiar velocities of the IGM gas, and its temperature; (ii) a source model that produces galactic Ly α emission, which accounts for the spatial distribution of LAEs and their emission profiles.

For step (i), the simulation of the IGM, we follow the procedure in Choudhury et al. (2015), hereafter referred to as CPBH15. This approach starts from a cosmological hydrodynamic simulation and then applies the excursion set formalism (Furlanetto, Zaldarriaga & Hernquist 2004; Zahn et al. 2007; Mesinger, Furlanetto & Cen 2011) to determine the large-scale ionization structure. We apply a self-shielding prescription that models the occurrence of neutral hydrogen embedded in ionized regions. Our reionization simulations are then calibrated to three different reionization histories, spanning the range consistent with CMB and Ly α forest data. This first step of the simulation is outlined in Sections 2.1 through 2.3. For step (ii), the source model, we also start with the same basic model used in CPBH15, aiming to reproduce their results. We then extend this basic model to try to account for differences between bright and faint LAEs. The details of these source models are outlined in Section 4.2.

2.1 Large-scale ionization structure

The underlying cosmological hydrodynamical simulation used in this work is taken from the Sherwood simulation suite (Bolton et al. 2017), initially run as part of a PRACE simulation program. These simulations were run using a modified version of the P-GADGET-3 TreePM smoothed particle hydrodynamics (SPH) code, itself an

updated version of GADGET-2 (Springel, Yoshida & White 2001; Springel 2005). Dark matter haloes were found on the fly using a Friends-of-Friends algorithm, with a minimum particle number of 32. The ΛCDM parameters used for this run (and hereafter in this work) are based on the Planck Collaboration XVI (2014) results: $h = 0.678$, $\Omega_m = 0.308$, $\Omega_\Lambda = 0.692$, $\Omega_b = 0.0482$, $\sigma_8 = 0.829$, $n = 0.961$, and $Y_{He} = 0.24$. The simulation used for this work was performed in a box of length $L = 160$ cMpc/h[1] (where prefix c indicates co-moving, and prefix p indicates proper). The runs were started with 2048^3 particles of gas and dark matter each ($N = 2 \times 2048^3$ total), giving a dark matter mass resolution of $M_{DM} = 3.44 \times 10^7$ $M_\odot$/h. The gravitational softening length was set at $l_{soft} = 3.13$ ckpc h^{-1}. Snapshots of the initial PRACE run were saved for redshifts in the epoch of interest at $z = 6.0$, 7.0, 8.0, and 10.0. We have also re-run the simulation in order to better sample the EoR, saving snapshots every 40 Myr; in particular, in this work we make use of snapshots at $5.756 \leq z \leq 9.546$.

Alongside the hydrodynamical and gravitational evolution of the gas and dark matter, the simulation included photoionization and photoheating calculated using the spatially uniform background from Haardt & Madau (2012).[2]

Note that for these simulations, the QUICK_LYALPHA star formation implementation in P-GADGET-3 was used. This option speeds up the simulation by converting gas particles (with temperatures lower than 10^5 *K* and overdensities larger than a thousand times the mean baryonic density) into collisionless star particles (Viel, Haehnelt & Springel 2004). For use in calculations, the densities, velocities, and temperatures of the particles were projected onto a grid using the SPH kernel. A projected slice of the density field from the simulation at redshift $z = 7$ can be seen in the left-hand panel of Fig. 1.

In CPBH15, a hybrid simulation was employed, comprised an $L = 10$ cMpc h^{-1}, $N = 2 \times 512^3$ P-GADGET-3 hydrodynamical simulation to model the hydrogen distribution, and a larger low-resolution dark matter-only simulation with $L = 100$ cMpc h^{-1}, $N = 1200^3$. These simulations were combined by tiling the small simulation box across the larger volume, making use of the ionization structure and large-scale velocity modes of the large simulation box. We take advantage here of the much higher dynamic range of the Sherwood simulation suite and employ instead a single hydrodynamical simulation with almost twice the volume of their hybrid simulation but at a factor 2 reduced spatial resolution compared to their 10 cMpc h^{-1} sized hydrodynamical simulation. Although lower in resolution, this has the advantage of retaining the correlation between the gas density fields and the halo structure of the simulation, which was not present in the hybrid simulation of CPBH15. The larger volume also allows us to probe to higher halo masses, which is key to our modelling of bright and faint LAEs.

In recent observations, Konno et al. (2018) surveyed co-moving volumes of $\sim 1.2 \times 10^7$ Mpc^3; our simulation volume ($\sim 1.3 \times 10^7$ Mpc^3) is therefore a better representation than the smaller volume of CPBH15 ($\sim 0.3 \times 10^7$ Mpc^3). In Fig. 1, we show a representative survey area with a red dashed square for comparison with our box size.

[1]For test cases to compare with CPBH15, we also used a box of length $L = 80$ cMpc h^{-1}.

[2]At lower redshifts not considered here, the photoheating rates were somewhat modified to better match the temperature measurements of Becker et al. (2011).

To generate the large-scale ionization structure of the simulation, we apply an excursion set method (Furlanetto et al. 2004; Mesinger & Furlanetto 2007; Choudhury, Haehnelt & Regan 2009; Santos et al. 2010; Mesinger et al. 2011; Hassan et al. 2016). This is a semi-analytic approach, which has been found to reproduce ionization fields that agree with low-resolution radiative transfer simulations (e.g. in Majumdar et al. 2014), whilst being computationally efficient. The first step assigns to haloes an emissivity as a function of their mass. In this work, we assume a linear relationship, with the number of ionizing photons produced by a halo, $N_\gamma = c_\gamma M_h$, with c_γ a constant of proportionality. Although recent observations of high-redshift UV luminosity functions may suggest non-linear scalings (e.g. Mason, Trenti & Treu 2015), this simplifying assumption should not have a strong effect on our modelling. In earlier work, such a linear scaling for the ionizing photon budget with mass has been found to approximately reproduce the high-redshift UV luminosity functions (Trenti et al. 2010). We note that non-linear models were used by Kulkarni et al. (2016) in the same reionization framework used here but were not found to have a strong effect on the resulting reionization history. Furthermore, Chardin et al. (2015) employed full radiative transfer simulations, modelling the ionizing luminosity with a similar linear scaling, and they were able to reproduce observations of the end of reionization very well. Physically, this simplifying assumption of a linear scaling may break down if galactic outflows or feedback alters the dependence (Finlator, Oppenheimer & Davé 2011). We do not impose a minimum mass of star-forming haloes but use the entire halo population of the simulation. Note that at least initially the value of c_γ is not important because of the later calibration scheme (see Section 2.3). Using this relationship, we establish a radiation field based on the locations and masses of the haloes in the simulation. We then flag a cell in the box, **i**, as ionized if there is some radius R inside which the condition,

$$\langle n_\gamma(\mathbf{i})\rangle_R > \langle n_H(\mathbf{i})\rangle_R\,(1+\overline{N}_{rec}), \tag{1}$$

is satisfied. Here n_γ and n_H are the photon and hydrogen (co-moving) number densities, respectively. The averages are taken over a spherical region of radius R centred on the cell. This condition is therefore comparing the number of ionizing photons in the neighbourhood of the cell (at a given scale R) to the number of hydrogen atoms in the same region, and if it is larger for some value of R then we flag that cell as being ionized. The factor of $1+\overline{N}_{rec}$ accounts for recombinations, where $\overline{N}_{rec}$ is the average number of recombinations per hydrogen atom that occur in the IGM. An equivalent statement of the condition in equation (1) is that a cell will be ionized if (Choudhury et al. 2009),

$$\zeta_{eff}\, f_{coll}(\mathbf{i}, R) \geq 1, \tag{2}$$

where $\zeta_{eff} = c_\gamma m_H \left((1+\overline{N}_{rec})(1-Y_{He})\right)^{-1}$ is an efficiency parameter and f_{coll} is the collapsed mass within a spherical volume of radius R given by

$$f_{coll}(R) = \frac{1}{\overline{\rho}(R)} \int_{M_{min}}^{\infty} dM \left.\frac{dn}{dM}\right|_R M. \tag{3}$$

In equation (3), $\overline{\rho}(R)$ is the average matter density within a radius R. Note that to go from equation (1) to equation (3), we have used the linear relationship for $N_\gamma(M)$. The constant of proportionality, c_γ, and the recombination factor have been absorbed into ζ_{eff}. This ionization efficiency parameter controls the size of ionized bubbles and must be calibrated so that the mass-averaged neutral fraction, Q_M matches the desired reionization history. Using the above prescription, we can determine for each cell in the simulation whether

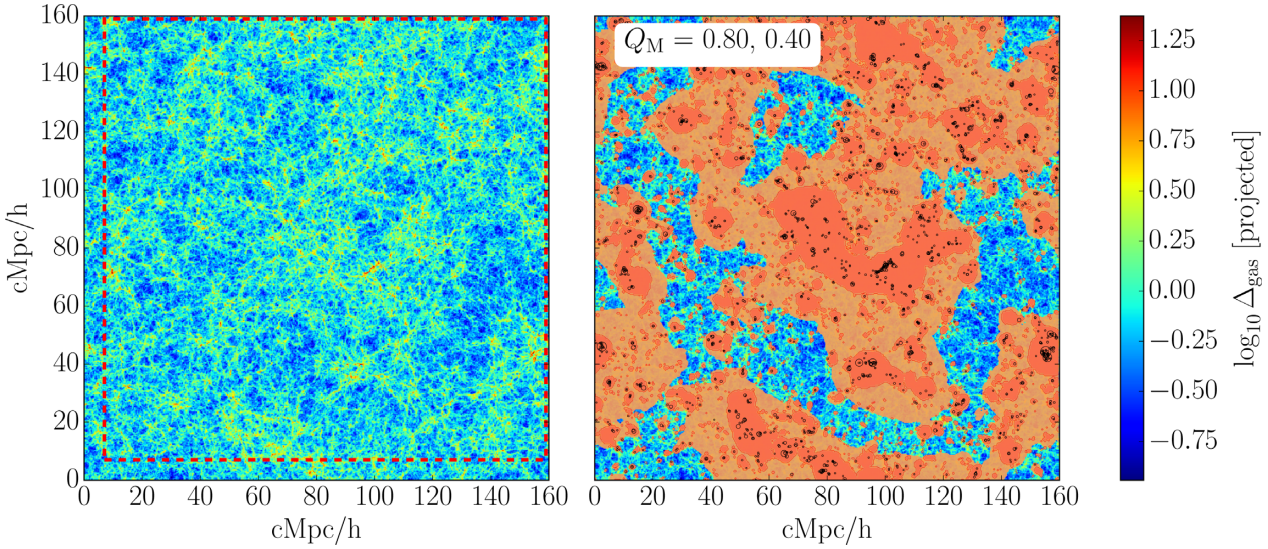

Figure 1. Gas overdensity (left) and ionization field (right, shaded) in a projected 0.5 cMpc h^{-1} slice of the $L = 160$, $N = 2048^3$, and $z = 7$ snapshot from the Sherwood suite. The density has been interpolated onto a uniform 3D grid using the SPH kernel, and then a thin slice has been projected to create the 2D map. The dashed red square is a representative area for the co-moving volume surveyed by Konno et al. (2018). For the ionization structure on the right-hand panel, the mass-averaged ionized fraction has been set to values of $Q_M = 0.8$ and 0.4. The shaded areas mark ionized regions (found using the excursion set method) with the darker (brighter) shade showing the $Q_M = 0.4$ (0.8) case. The positions of haloes from this slice are shown in black, with marker size proportional to halo mass.

it is ionized. For those cells that are not ionized, we set the neutral fraction to $x_{HI} = 1$. If a cell is ionized, then its neutral fraction is found assuming photoionization equilibrium (Meiksin 2009),

$$x_{HI}(\mathbf{i}) = \frac{n_e(\mathbf{i})\,\alpha_B(T)}{\Gamma_{HI} + n_e(\mathbf{i})\,\alpha_B(T)}, \tag{4}$$

where n_e is the free electron number density, $\alpha_B(T)$ is the case B recombination rate, and Γ_{HI} is the background photoionization rate. Note that here we make the simplifying assumption of a spatially uniform background photoionization rate (within ionized regions). In reality, however, the varying position of sources and the inhomogeneous distribution of matter should lead to a non-uniform background. To include this effect properly, would require full radiative transfer calculations. We explore how varying the photoionization rate can affect LAE visibility in Section 6.2. This suggests that an inhomogeneous UV background could lead to fluctuations in the Ly α transmission from halo to halo, but it is expected that this would be subdominant to the average evolution driven by the IGM. The values of Q_M and Γ_{HI} are found during the calibration stage, such that the simulation is consistent with a desired reionization history.

In the right-hand panel of Fig. 1, we show the ionization field for two different ionized fractions: in dark orange, we show the ionized regions for $Q_M = 0.4$, whilst the lighter orange region is at a higher fraction of $Q_M = 0.8$. The positions of the haloes are overplotted as empty black circles, with the size of the marker proportional to the halo mass. As expected from the excursion set construction, the largest haloes sit in and dominate the largest ionized regions.

2.2 The self-shielding of dense gas in ionized regions

The excursion set method described above is effective at producing the large-scale ionization field; however, one of its most significant limitations is modelling dense self-shielded clumps within already (re-)ionized regions. In order to account for such regions, we employ a prescription based on the overdensity of hydrogen, Δ_H, in the hydrodynamical simulation. The prescription we use is based on the results of Chardin, Kulkarni & Haehnelt (2018), a modified version of those found in Rahmati et al. (2013) that aims to reproduce the self-shielding of dense regions within ionized bubbles during reionization. Here we apply the same ionization equilibrium approach from equation (4), but the local photoionization rate is modified to the empirical fit of Rahmati et al. (2013),

$$\frac{\Gamma_{HI}(\mathbf{i})}{\Gamma_{HI,\,global}} = (1 - f(z))\left[1 + \left(\frac{\Delta_H}{\Delta_{ss}}\right)^{\beta(z)}\right]^{\alpha_1(z)} + f(z)\left[1 + \left(\frac{\Delta_H}{\Delta_{ss}}\right)\right]^{\alpha_2(z)}, \tag{5}$$

where Δ_{ss} is the overdensity threshold for self-shielding, and f, β, α_1, and α_2 are the redshift-dependent parameters found by Chardin et al. (2018). We use the threshold found by Chardin et al. (2018), scaled appropriately by photoionization rate. We note that they found that the self-shielding threshold is in reasonable agreement with the parametrization found by considering the local Jeans length (Schaye 2001; Furlanetto et al. 2005),

$$\Delta_{ss} = 36\left(\frac{\Gamma_{HI}}{10^{-12}s^{-1}}\right)^{2/3}\left(\frac{T}{10^4K}\right)^{2/15}\left(\frac{\mu}{0.61}\right)^{1/3} \times \left(\frac{f_e}{1.08}\right)^{-2/3}\left(\frac{1+z}{8}\right)^{-3}, \tag{6}$$

where μ is the mean molecular weight. Our default prescription does have a higher self-shielding threshold than was found for the 'SS-R' case of CPBH15, in which they followed the Rahmati et al. (2013) prescription. This means that self-shielding plays a less dominant role in our models. We explore the effect of changing this prescription in Section 6.2.

2.3 Calibrating the simulations for different reionization histories

The methodology described above creates a realistic large-scale ionization field, as well as an accurate neutral hydrogen distribution within ionized bubbles. The model has two free parameters, however, $\Gamma_{\rm HI}$ and $Q_{\rm M}$, which need to be calibrated so that the simulation matches observational constraints. In order to calibrate these two quantities self-consistently, we iteratively solve the equation (Choudhury 2009; Kulkarni et al. 2016),

$$\frac{dQ_{\rm M}}{dt} = \frac{\langle \dot{n}_{\rm ion} \rangle - \langle \dot{n}_{\rm rec} \rangle}{n_{\rm H}}, \tag{7}$$

where $Q_{\rm M}$ is the *mass-averaged* neutral fraction within the simulation box. We solve this equation by starting with the desired $Q_{\rm M}$ and a guessed $\Gamma_{\rm HI}$. This allows us to estimate the co-moving emissivity (Kuhlen & Faucher-Giguère 2012; Becker & Bolton 2013),

$$\langle \dot{n}_{\rm ion} \rangle = \frac{\Gamma_{\rm HI} Q_{\rm V}}{(1+z)^2 \sigma_{\rm H} \lambda_{\rm mfp}} \left(\frac{\alpha_{\rm b} + 3}{\alpha_{\rm s}} \right), \tag{8}$$

where $Q_{\rm V}$ is the *volume-averaged* neutral fraction, $\sigma_{\rm H}$ is the hydrogen photoionization cross-section at 912 Å, $\lambda_{\rm mfp}$ is the mean free path of ionizing radiation at the same wavelength, and the bracketed factor includes the spectral indices for ionizing sources $\alpha_{\rm s}$ and the ionizing background $\alpha_{\rm b}$. Note that in the simulation, we calculate the mass and volume averaged neutral fractions by summing over the neutral fraction in each projected grid cell, $q(\mathbf{i})$, with the appropriate weighting,

$$Q_{\rm M} = \frac{1}{M_{\rm tot}} \sum_{\mathbf{i}} M(\mathbf{i}) q(\mathbf{i}) = \frac{1}{\rho_{\rm tot}} \sum_{\mathbf{i}} \rho(\mathbf{i}) q(\mathbf{i}), \tag{9}$$

$$Q_{\rm V} = \frac{1}{N} \sum_{\mathbf{i}} q(\mathbf{i}), \tag{10}$$

where $M(\mathbf{i})$, $\rho(\mathbf{i})$ are the mass and density in a given cell, the total mass and density are $M_{\rm tot} = \sum_{\mathbf{i}} M(\mathbf{i})$ and $\rho_{\rm tot} = \sum_{\mathbf{i}} \rho(\mathbf{i})$, respectively, and N is the total number of cells (e.g. 2048^3). These expressions are valid here because of the uniform grid projection.

The mean free path is fixed to the predicted values of a given reionization history model (see Section 4). We found this to be more stable than trying to calculate the mean free path iteratively from the simulation using equation (7). To test that this was not sensitive to the resolution needed to properly resolve the self-shielded regions such as damped Ly α absorbers (DLAs) and Lyman-limit systems (LLSs), we calculated the mean free path from the simulation for a fixed photoionization rate. Our calculations are indeed converged with respect to the predicted values from the models. This suggests that although we have to fix the mean free path for the calibration, we do properly resolve the self-shielded systems.

The bracketed term on the right side of equation (8) is determined by the spectrum of ionizing radiation; in this work, we use the same value as used by Haardt & Madau (2012). During the iterative solving of equation (7), we also find the globally averaged co-moving rate of recombinations given by

$$\langle \dot{n}_{\rm rec} \rangle = \frac{1}{N} \sum_{\mathbf{i}} \alpha_{\rm B} (1+z)^3 \, n_{\rm e}(\mathbf{i}) \, n_{\rm HII}(\mathbf{i}) \tag{11}$$

$$\simeq \frac{1}{N} \sum_{\mathbf{i}} \alpha_{\rm B} (1+z)^3 \, f_{\rm e} \, n^2_{\rm HII}(\mathbf{i}), \tag{12}$$

where $\alpha_{\rm B}$ is the (case-B) recombination rate, and $f_{\rm e} = 1.08$ is the number of electrons per hydrogen nucleus.[3]

In summary, the calibration method takes as input the values for $Q_{\rm M}(z)$ and $\lambda_{\rm mfp}(z)$ from each reionization history model and then uses the large-scale ionization field (constructed via the excursion set method) to solve for an equilibrium $\Gamma_{\rm HI}$ that satisfies equation (7).

3 LYMAN-α TRANSMISSION

Having performed the calibration as detailed in Section 2.3, we have simulation snapshots with realistic neutral hydrogen distributions that can be used to test the effect of the CGM and the IGM on the transmission of the Ly α radiation from LAEs.

Early galaxies with high star-formation rates (SFRs) produce ionizing radiation in their stellar component (Partridge & Peebles 1967). This ionizing radiation is then converted into Ly α line emission through recombination and collisional excitation of the gas in the ISM (Charlot & Fall 1993; Dijkstra 2014). The radiative transfer of Ly α photons through the ISM and CGM causes a diffusion in both physical and frequency space, resulting in a significant change to the emission profile. The photons that escape the galaxy must then traverse the IGM, which at $z > 6$ contains a significant non-zero neutral hydrogen fraction. Due to the resonant nature of Ly α absorption in neutral hydrogen, the presence of even small neutral fractions can alter the visibility of LAEs (see Meiksin 2009; Dijkstra 2014, for reviews of IGM and Ly α physics).

As discussed in Section 1, observations of LAEs at high redshifts have found a decline in number densities. Explaining these observations is made difficult by the degeneracy between internal galaxy evolution (parametrized by the fraction of Ly α photons that escape galaxies, $f_{\rm esc,\,Ly\,\alpha}$, which may be a function of z) and IGM absorption (parametrized by the neutral fraction $x_{\rm HI}$) (Dayal et al. 2009). In this work, we consider the effect of the CGM/IGM only and do not model galaxy evolution.

3.1 Ly α transmission fraction

In order to quantify the effect of the IGM and the CGM on the transmission of Ly α photons, we extract sightlines from our simulation snapshots that pass through LAE host haloes and calculate the radiative transfer along them (see Section 4 for details on how LAE host haloes are selected). The sightlines are chosen to be 160 cMpc $\rm h^{-1}$ in length, parallel to the simulation box axes. We take advantage of the periodic boundary conditions of the simulation to translate the start of the sightline such that the halo is positioned at the centre.[4] The gas properties are initially gridded into 2048 bins (78.13 ckpc $\rm h^{-1}$ bin resolution), with a further 2048 bins in a high-resolution region of length 20 cMpc $\rm h^{-1}$ (giving 9.77 ckpc $\rm h^{-1}$ bin resolution) containing the host halo.[5] This ensures that we resolve the gas around the host halo, including small-scale high-density regions likely to self-shield.

Neglecting scattering by dust, the equation of radiative transfer can be written (Draine 2011),

$$J_\nu(\tau_\nu) = J_\nu(0) e^{-\tau_\nu} + \int_0^{\tau_\nu} d\tau'_\nu \, e^{-(\tau_\nu - \tau'_\nu)} \, S_\nu(\tau'_\nu), \tag{13}$$

[3] Note $f_{\rm e} > 1$ due to singly ionized helium in the H ii regions.
[4] The optical depth calculation was found to converge on considerably smaller spatial scales than 80 cMpc $\rm h^{-1}$.
[5] We note that the softening length used in these simulations is 3.13 ckpc $\rm h^{-1}$.

$$= J_\nu(0)\mathrm{e}^{-\tau_\nu}, \tag{14}$$

where $J(\nu)$ is the galaxy emission profile (the specific intensity of radiation at frequency ν), $\tau(\nu)$ is the Ly α optical depth (see sub-Section 3.2 below), and the source function, S_ν, is approximately zero because the Ly α emissivity of the IGM gas is negligible (Silva, Kooistra & Zaroubi 2016). This expression allows us to calculate the emission profile of a galaxy after reprocessing by the surrounding IGM gas, $J'(\nu) = J(\nu)\mathrm{e}^{-\tau(\nu)}$. With this we can calculate the transmission fraction of photons (or transmissivity) given by (Mesinger et al. 2015)

$$T^{\rm IGM}_{{\rm Ly}\alpha} = \frac{\int_{\nu_{\rm min}}^{\nu_{\rm max}} d\nu\, J(\nu)\, \mathrm{e}^{-\tau(\nu)}}{\int_{\nu_{\rm min}}^{\nu_{\rm max}} d\nu\, J(\nu)}, \tag{15}$$

where $J(\nu)$ is appropriately normalized. Since we place the Ly α emitter at the centre of the sightline, the frequency limits in equation (15) used in this work are the Ly α frequency blue/redshifted along half the sightline length, which extends considerably beyond the wings of the emission profile.

We note that this '$\mathrm{e}^{-\tau}$ modelling' of the radiative transfer of Ly α photons has been compared to full radiative transfer by Zheng et al. (2010). They suggested that such models can overattenuate the line profile compared to that of full calculations because some of the frequency diffusion is neglected. A balance has to be struck between the frequency diffusion in the inner parts of the galaxy and the attenuation by the neutral hydrogen surrounding the galaxy. We will account for the frequency diffusion in the inner part of the galaxies in our modelling of the spectral distribution (see Section 4).

3.2 Ly α attenuation due to the CGM and IGM

As suggested in Dijkstra (2014), we split the Ly α optical depth responsible for attenuating the Ly α emission from galaxies into two contributions: (i) $\tau_{\rm HI}(z, v)$, the opacity due to any recombined neutral hydrogen or self-shielded regions *within* ionized bubbles; (ii) $\tau_{\rm D}(z, v)$, the opacity due to damping-wing absorption in the residual neutral IGM. Note that these quantities depend on the velocity offset, v, which is determined by both the Hubble flow and the difference in peculiar velocity of emitter and absorber. So we can calculate

$$\tau_{{\rm Ly}\alpha}(v) = \tau_{\rm HI}(v) + \tau_{\rm D}(v). \tag{16}$$

Physically, photons emitted close to line centre will redshift out of resonance as they traverse the IGM. It is important to consider that scattering/absorption occurs at velocity shifts close to zero in the absorber's rest frame. This means that redshifted photons in the frame of neutral gas infalling onto the host halo can be blueshifted back into resonance.

We note that both of the components in equation (16) are calculated in the same manner. In order to calculate the optical depth, we assume a Voigt profile for the absorption cross-section, in particular, using the analytic approximation from Tepper-García (2006),

$$H(a,x) = \mathrm{e}^{-x^2} - \frac{a}{\sqrt{\pi}x^2}[\mathrm{e}^{-2x^2}(4x^4+7x^2+4+1.5x^{-2}) - 1.5x^{-2} - 1], \tag{17}$$

where $H(a, x)$ is the Hjerting function, related to the Voigt profile by (Rybicki & Lightman 1985)

$$\phi(\nu) = (\Delta\nu_{\rm D})^{-1}\pi^{-1/2}H(a,x), \tag{18}$$

where $\Delta\nu_{\rm D} \equiv \frac{\nu_\alpha}{c}\sqrt{\frac{2k_{\rm B}T}{m_{\rm H}}}$, (19)

$$a \equiv \frac{\Lambda_\alpha}{4\pi\Delta\nu_{\rm D}}, \tag{20}$$

$$x \equiv \frac{\nu-\nu_\alpha}{\Delta\nu_{\rm D}}. \tag{21}$$

Note in the above formulae we have used: the Ly α frequency $\nu_\alpha = 2.46 \times 10^{15}$Hz, the hydrogen $2p \rightarrow 1$ s decay rate $\Lambda_\alpha = 6.25 \times 10^8 \mathrm{s}^{-1}$, the Boltzman constant $k_{\rm B}$, the hydrogen atomic mass $m_{\rm H}$, and the temperature of the gas, T, at the absorber. For a given sightline, we find the optical depth in a (redshift space) cell **i** by summing up all the contributions from positions in front of the emitter (Bolton & Haehnelt 2007), where we define $v = 0$ at the position of the emitter,

$$\tau(\mathbf{i}) = \frac{\nu_\alpha\sigma_\alpha\delta R}{\sqrt{\pi}}\sum_j^N \frac{n_{\rm HI}(j)}{\Delta\nu_{\rm D}(j)}H(a, x(i,j)), \tag{22}$$

where δR is the cell width, and the cell has Hubble velocity $v_{\rm H}(\mathbf{i})$ and peculiar velocity $v_{\rm pec}(\mathbf{i})$, such that

$$x(i,j) = \sqrt{\frac{m_{\rm H}}{2k_{\rm B}T}}\,[v_{\rm H}(\mathbf{i}) - v_{\rm H}(\mathbf{j}) - v_{\rm pec}(\mathbf{j})]. \tag{23}$$

Equation (22) is the optical depth to Ly α emission from the halo position, which is then redshifted along the sightline. In velocity space absorption can appear to occur 'behind' the halo due to the non-negligible width of the absorption profile and because of infalling matter around the halo.

3.3 Ly α scattering in the host halo

The importance of carefully modelling the neutral gas in and close to the host halo was emphasized and explored in Sadoun et al. (2017), hereafter referred to as SZM17. In Fig. 2, we show spherically averaged density profiles for three mass bins spanning the masses of the halo population in our simulations. The neutral hydrogen densities were calculated assuming a fixed value of $\Gamma_{\rm HI}$ and solving for photoionization equilibrium using equation (4), including the self-shielding prescription discussed in Section 2.2. Note, however, that spherically averaging will smooth out the overdensities surrounding the halo, which are used to calculate the amount of self-shielding; this means that these radial profiles somewhat underrepresent the neutral gas density compared to sightlines through our simulations that are not spherically averaged. We see more extended profiles in the more massive haloes, whereas in the less massive haloes, the profiles are more peaked around the central halo position. In the central panel, we also compare to profiles presented for haloes with mass $M_{\rm h} = 10^{10.5}\,\mathrm{M}_\odot$ by SZM17. We note that the total hydrogen density profiles are similar for $r > 20$ pkpc; however, at smaller radii both our total and neutral hydrogen densities are lower than the model presented by SZM17. This is likely due to the `QUICK_LYALPHA` star-formation prescription, which converts dense gas into star particles (as described in Section 2.1). This prescription will therefore remove some of the very dense gas in the centres of haloes, as we see in Fig. 2.

We also show the neutral hydrogen profiles for the widely used self-shielding prescription proposed by Rahmati et al. (2013) with the thin (step) curves. These are closer to those presented by SZM17, especially for the lower photoionization rate of $\Gamma_{\rm HI} = 10^{-14}$ s^{-1}.

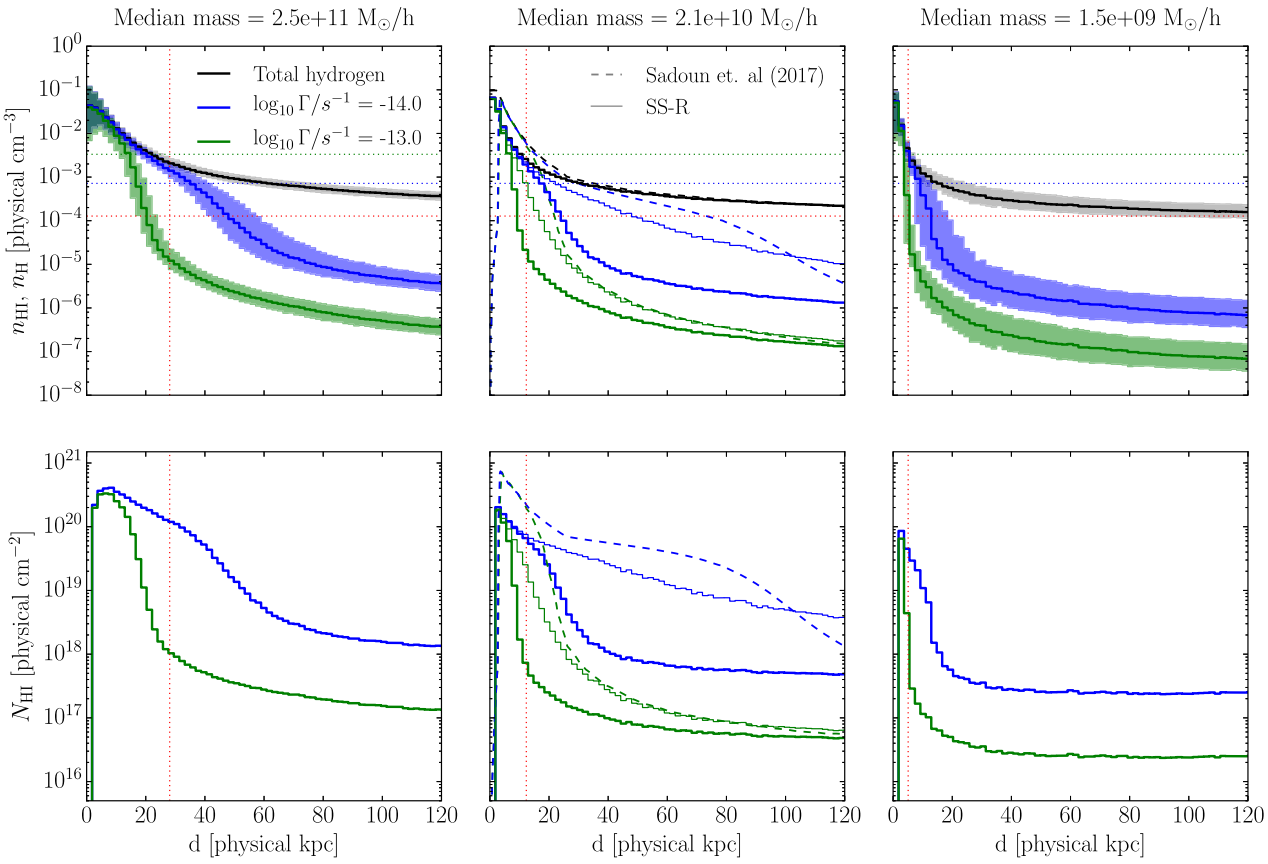

Figure 2. *Top panels*: Median hydrogen number density profiles at $z = 7$, spherically averaged, for both total hydrogen in black and neutral hydrogen in green ($\Gamma = 10^{-13}$ s^{-1}) and blue ($\Gamma = 10^{-14}$ s^{-1}). The three panels correspond to samples of 500 haloes with mass bins that bracket the halo population of our simulations: most massive on the left, least massive on the right, and a sample chosen for comparison with SZM17's $M_{\rm h} = 10^{10.5}$ M$_\odot$ model in the middle panel. The red-vertical-dotted line shows the median virial radii, whilst the horizontal red line shows the mean baryonic density. The horizontal green- and blue-dotted lines show the self-shielding density thresholds for the different photoionization rates. In the middle panel, we also show the profiles from SZM17 with dashed lines and the profiles found using the Rahmati et al. (2013) self-shielding prescription (labelled SS-R) shown with thin stepped lines. The shaded regions indicate 68 per cent scatter in the samples (not shown in the middle panel to aid visual comparison with SZM17). *Bottom panels*: Column densities at a given radius estimated by multiplying the number density by the radial distance.

We suggest that most of the difference between the profiles in our simulations and the modelling of SZM17 is due the presence of ionizing sources. In the simulations on which the prescription of Chardin et al. (2018) is based, there are ionizing sources within the self-shielded regions that affect the local photoionization rate and therefore the self-shielding threshold density. These are not accounted for in the Rahmati et al. (2013) prescription. Note that while SZM17 do account for a central ionizing source in their calculation, they assume this source to be rather weak. As already mentioned, some of the difference will also be due to the spherical averaging that is not accounted for in our self-shielding prescription. Note further that in this work we also consider the role of the larger scale ionization structure, and the presence of an IGM volume-filling neutral fraction, which SZM17 neglect. As discussed by SZM17, the attenuation near to the host halo is very sensitive to the distribution of neutral hydrogen close to the Ly α emitters. We discuss this in more detail in Section 6.2.

CPBH15 and Bolton & Haehnelt (2013) did not attempt to simulate the complex radiative transfer within the host halo but instead assumed an intrinsic emission profile (for photons leaving the host system but before attenuation by the IGM) and argued that this accounts for these effects. In those works, the contributions of neutral gas within 20 pkpc were therefore neglected around the halo; for the narrower range of halo masses considered in those works, this was a consistent and sufficient exclusion. Our modelling here includes a considerably larger range of halo masses, which therefore also have a considerable range of virial radii. Excluding gas within a fixed distance of 20 pkpc uniformly across our halo population would remove all the neutral gas within a few virial radii around the less massive haloes, whilst only remove the gas within a fraction of the virial radius in the most massive haloes. Here we therefore choose the exclusion region based on the mass (or virial radius) of the host halo and will use our simulation and the e$^{-\tau}$ approach to account for the attenuation due to the neutral hydrogen in the outer part of the host haloes of Ly α emitters.

We have tested the effect of varying the size of the exclusion region by excluding gas within 0.5, 1.0, 2.0, 5.0, and 10.0 $R_{\rm vir}$, where we use $R_{\rm vir} = R_{200,\,\rm crit}$. The resulting transmission curves for these exclusions, calculated as described in Section 3.2, are shown in Fig. 3. In the left-hand panels in shades of blue, we present the results for a sample of less massive haloes, whilst in the right-hand panels in shades of red, we show the results for more massive haloes. The important role of the gas peculiar velocities can be seen in the top panels by comparing the solid lines (full calculations) to the dashed lines (calculated neglecting peculiar velocities). In particular, in the more massive haloes, the peculiar velocities are

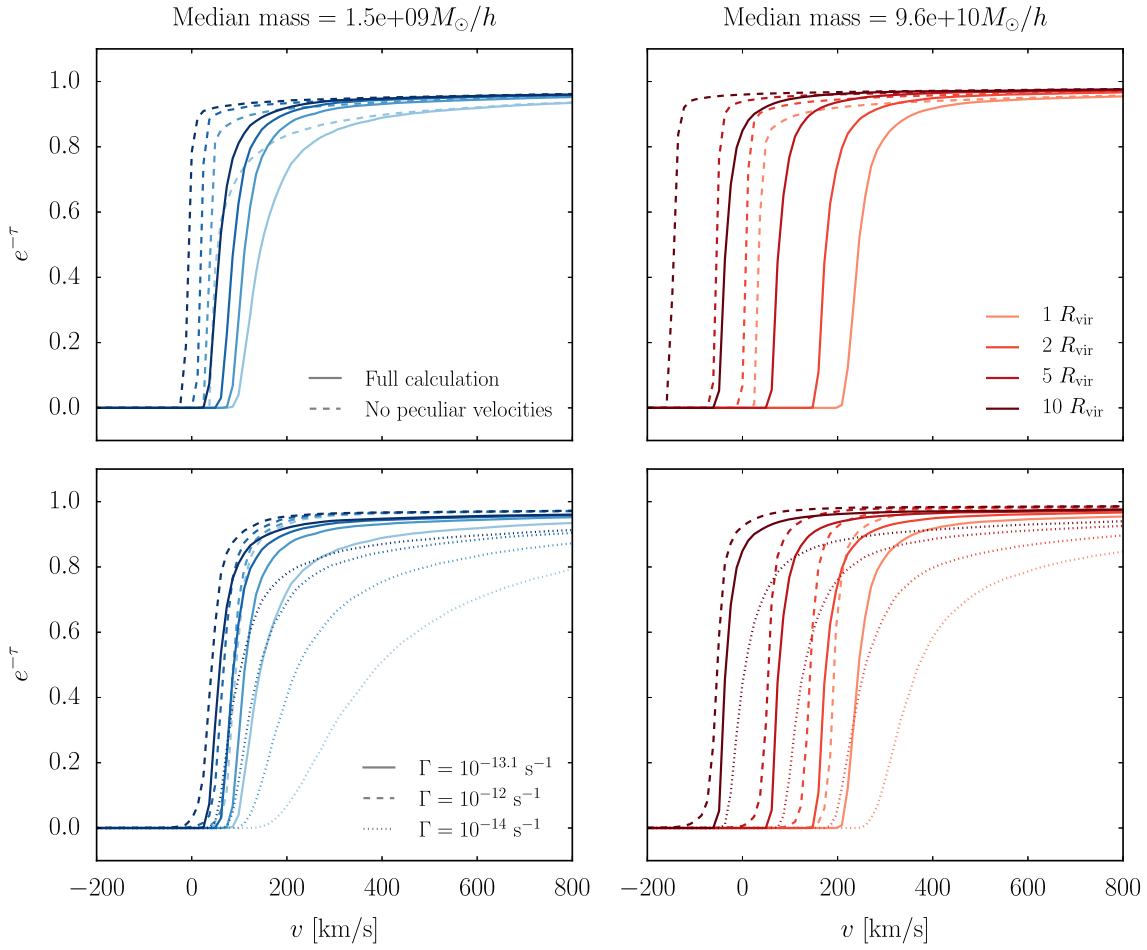

Figure 3. Median transmission curves, testing different exclusion radii (indicated by darkness of line), for a less massive sample of haloes (left-hand panels) and a more massive sample (right-hand panels). In the top panels, the solid lines show the results from the full calculation, whilst the dashed lines show what happens when peculiar velocities are neglected. Both of these panels assume $\log_{10}\Gamma/\mathrm{s}^{-1} = -13.1$. The bottom panels compare three different photoionization rates: $\log_{10}\Gamma/\mathrm{s}^{-1} = -12$ (dashed), -13.1 (solid), and -14 (dotted).

sufficient to dramatically move the position of the damping wing. We also note, considering the solid lines, that the more massive haloes are more sensitive to the choice of exclusion: in the less massive haloes (blue lines), the damping wing of the profile is moved by $\sim$150 km s^{-1} between the two exclusion extremes shown, whilst in the more massive haloes it is moved by $\sim$350 km s^{-1}.

In the bottom panels of Fig. 3, we show the effect of varying the chosen background photoionization rate Γ. This leads to a change in the amount of equilibrium neutral hydrogen (self-shielded or recombined) within ionized regions close to the halo. We see that for the higher photoionization rate, the effect of changing the exclusion region is reduced and vice versa for the lower photoionization rate.

Our fiducial choice is to exclude gas within 1.0 $R_{\rm vir}$; unless otherwise specified, all results presented hereafter were calculated with this choice. As can be seen in Fig. 3, there will be some dependence of the Ly α transmission on the chosen exclusion region. We mitigate this dependence with our choice of source models, as detailed in Section 4. Further consequences of our choice of the size of the exclusion region are discussed in Section 6.2.

3.4 Transmission fraction ratios

As we are primarily interested in the evolution of the Ly α attenuation during the epoch of reionization, we consider the ratio of transmission fractions $T(z)/T(z_{\rm ref})$ [hereafter referred to as transmission fraction ratios (TFRs)], where $z_{\rm ref}$ is a reference redshift. In particular, we choose to construct the ratio of higher redshifts with respect to $z_{\rm ref} = 5.756$, matching the choice of $z = 5.7$ common in the literature.

Narrow-band (Ly α-selected) observations of LAEs at different redshifts can be used to calculate the TFR evolution as (Konno et al. 2018)

$$\frac{\overline{T}(z)}{\overline{T}(z_{\rm ref})} = \frac{\kappa(z_{\rm ref})}{\kappa(z)} \frac{f_{\rm esc,Ly\alpha}(z_{\rm ref})}{f_{\rm esc,Ly\alpha}(z)} \frac{\rho_{\rm Ly\alpha}(z)/\rho_{\rm Ly\alpha}(z_{\rm ref})}{\rho_{\rm UV}(z)/\rho_{\rm UV}(z_{\rm ref})}, \quad (24)$$

where $L_{\rm Ly\,\alpha} = \kappa L_{\rm UV}$, $f_{\rm esc,\,Ly\,\alpha}$ is the escape fraction of Ly α photons, and $\rho_{\rm UV}$ is the intrinsic UV luminosity density whilst $\rho_{\rm Ly\,\alpha}$ is the observed (attenuated) Ly α luminosity density. This relative transmission fraction is an effective way of quantifying the evolution observed in the LAE luminosity function. In particular, it is a convenient quantity that allows one to estimate the neutral fraction $x_{\rm HI}$ from an observational sample. In this work, we also choose to calculate the TFR evolution rather than the luminosity function evolution because it can be calculated via equation (15) independently of the uncertain relationship between the LAE host halo's mass and its Ly α luminosity. We leave the explicit modelling of the $M_{\rm h}$–$L_{\rm Ly\,\alpha}$ relation, and hence the luminosity function evolution, to future work.

3.5 Ly α fractions

Alongside the evolution of the Ly α luminosity function, observers have also measured the evolution of the fraction of continuum-selected galaxies that emit strongly in Ly α. This is determined using samples of UV-selected galaxies (via the Lyman break technique), with follow-up spectroscopy to measure Ly α. The fraction, $X_{\mathrm{Ly}\,\alpha}$, is the proportion of such an LBG sample that is measured to have an Ly α-equivalent width above a given threshold (Stark et al. 2011; Ono et al. 2012; Treu et al. 2012).

In this work, we also calculate the predicted evolution of $X_{\mathrm{Ly}\,\alpha}$ following a similar strategy to Sadoun et al. (2017) and CPBH15. We start with the prescription of Dijkstra, Mesinger & Wyithe (2011) in which we derive the *rest-frame-equivalent width* (REW), $\mathcal{W}$, distribution. This is done by assuming that there is a probability distribution $P_{\mathrm{int}}(>\mathcal{W})$ for an intrinsic unabsorbed $\mathcal{W}$ distribution that does not evolve with redshift; the observed redshift evolution is then entirely due to the attenuation by the IGM. Given the probability distribution for the transmitted fractions at a given redshift $P_T(T, z)$ and the intrinsic distribution, we can find the REW distribution at that redshift as

$$P(>\mathcal{W}, z) = \int_0^1 \mathrm{d}T\; P_T(T, z)\, P_{\mathrm{int}}(>\mathcal{W}/T). \tag{25}$$

As in CPBH15, we choose to determine $P_{\mathrm{int}}(>\mathcal{W})$ as the function which gives $P(>\mathcal{W}, z = 6)$ that matches the observational data of Stark et al. (2011). We fit the following functional form for the intrinsic distribution (Shapley et al. 2003),

$$P_{\mathrm{int}}(>\mathcal{W}) = \exp(-\mathcal{W}/\mathcal{W}_0)/(\mathcal{W}_0 + \mathcal{W}_1), \tag{26}$$

where $\mathcal{W}_0$ and $\mathcal{W}_1$ are free parameters that vary depending on the simulated transmission fraction distribution. Given this intrinsic distribution, and using equation (25), we can find the fraction of LAEs over a given threshold equivalent width as

$$X_{\mathrm{Ly}\alpha}(\mathcal{W}, z) = P(>\mathcal{W}, z). \tag{27}$$

The values predicted by the simulations can then be compared to observed fractions.

4 MODELS

Using the above simulation set-up and Ly α transmission framework, we can explore different models of reionization and LAEs to compare with current observations. In particular, we test three reionization histories that bracket the possible progress of reionization at a given redshift. We also employ three different models for the masses of the host haloes of LAEs to explore the effect of host halo mass on Ly α transmission. We therefore test a total of nine possible model combinations. Further variations we have considered are described in Appendix B.

4.1 Reionization histories

We consider here three different reionization histories first discussed in CPBH15; we follow the naming convention established in Kulkarni et al. (2016). As outlined in Section 2.3, each model provides $Q_{\mathrm{M}}(z)$ and $\lambda_{\mathrm{mfp}}(z)$ which we input into the calibration calculation.

(i) **HM12**: This ionization history corresponds to the commonly used model of Haardt & Madau (2012), based on the meta-galactic UV background. We use $Q_{\mathrm{M}}(z)$ and $\lambda_{\mathrm{mfp}}(z)$ as predicted in Haardt & Madau (2012). In this model, the galactic UV emission is used as a tracer of the cosmic star formation history; this can be derived from the galaxy UV luminosity function (Robertson et al. 2013). Importantly, the main contribution to the ionizing photon budget comes from galaxies, with quasars and early Population III stars playing a negligible role. The universe is completely ionized in this model by $z = 6.7$. Comparing the model predictions to observed data, it agrees reasonably well with observed background photoionization rates (Faucher-Giguère et al. 2009; Calverley et al. 2011; Wyithe & Bolton 2011). However, its prediction for the Thomson optical depth of the CMB, $\tau_{\mathrm{el}} = 0.084$, is higher than the measurement of Planck Collaboration XLVII (2016) by more than $1\,\sigma$.

(ii) **Late**: This model uses the same evolution as the HM12 model with $Q(z)$ shifted in z such that reionization completes at $z = 6$ instead of $z = 6.7$, but with the same dQ_{M}/dz. A similar reionization history was found in the full radiative transfer simulations of Chardin et al. (2015), hereafter referred to as Ch15. In Ch15, the radiative transfer code ATON (Aubert & Teyssier 2008) was used to post-process high-resolution cosmological hydrodynamical simulations calibrated to Ly α forest data in order to calculate the evolution of the ionizing photon mean free path. We use the mean free path predicted in that work for our calibration. The CMB Thomson optical depth is $\tau_{\mathrm{el}} = 0.068$ in this model.

(iii) **Very Late**: Reionization completes at $z = 6$ as in the Late model, but the evolution of Q_{M} is much more rapid for $z > 6$. AGN-dominated reionization could lead to the history that this model predicts; see Kulkarni et al. (2017) for further details. We predict the mean free path for this model using the relationship between Q_{M} and λ_{mfp} from the Late model.[6] The Thomson optical depth in this case is $\tau_{\mathrm{el}} = 0.055$.

We follow Kulkarni et al. (2016) in choosing the Late reionization history as our fiducial model.

In Fig. 4, we show the final calibrated parameters of the simulation, including the reionization histories for $Q_{\mathrm{M}}(z)$. The HM12, Late and Very Late calibrated parameters are shown as blue circles, red triangles, and grey inverted triangles, respectively, in all panels. The solid black lines in all panels show the predictions of the underlying model from HM12 (Haardt & Madau 2012), whilst the red dashed lines show the predictions from Ch15 (Chardin et al. 2015). The fixed quantities are $Q_{\mathrm{M}}(z)$ and $\lambda_{\mathrm{mfp}}(z)$, shown on the left-most panels. We see that reionization progresses from high redshift (where $Q_{\mathrm{M}} \to 0$) until around $z \sim 6$; specifically in the HM12 model, we see $Q_{\mathrm{M}} = 1$ at $z = 6.7$, whilst in the other models, it reaches 1 at $z = 6$. The optical depth of the CMB to electron scattering is predicted by the reionization history models, shown in the top middle panel. Here the three lines for each model can be compared to the Planck Collaboration XLVII (2016) value shown as a horizontal green line, with green shading indicating the $1\,\sigma$ bounds. The quantities derived during our self-consistent calibration are the clumping factor (bottom middle panel), the ionizing emissivity (bottom right panel), and the background photoionization rate (top right panel). We see in the HM12 model that the mean free path and the photoionization rate increase at a largely constant exponential rate as reionization progresses, with a roughly constant ionizing emissivity. This smooth evolution of the mean free path may, however, be unrealistic (Puchwein et al. 2018). In comparison, the Late and Very Late models predict a more steady photoionization rate at high redshifts, which suddenly increases close to percolation at $z \sim 7$ when the H II regions overlap to an extent that the mean free path

[6] Beyond $z = 6$, both of these quantities are monotonically increasing with redshift and hence can be mapped together. This allows us to find the mean free path for a given Q_{M} of the Very Late model.

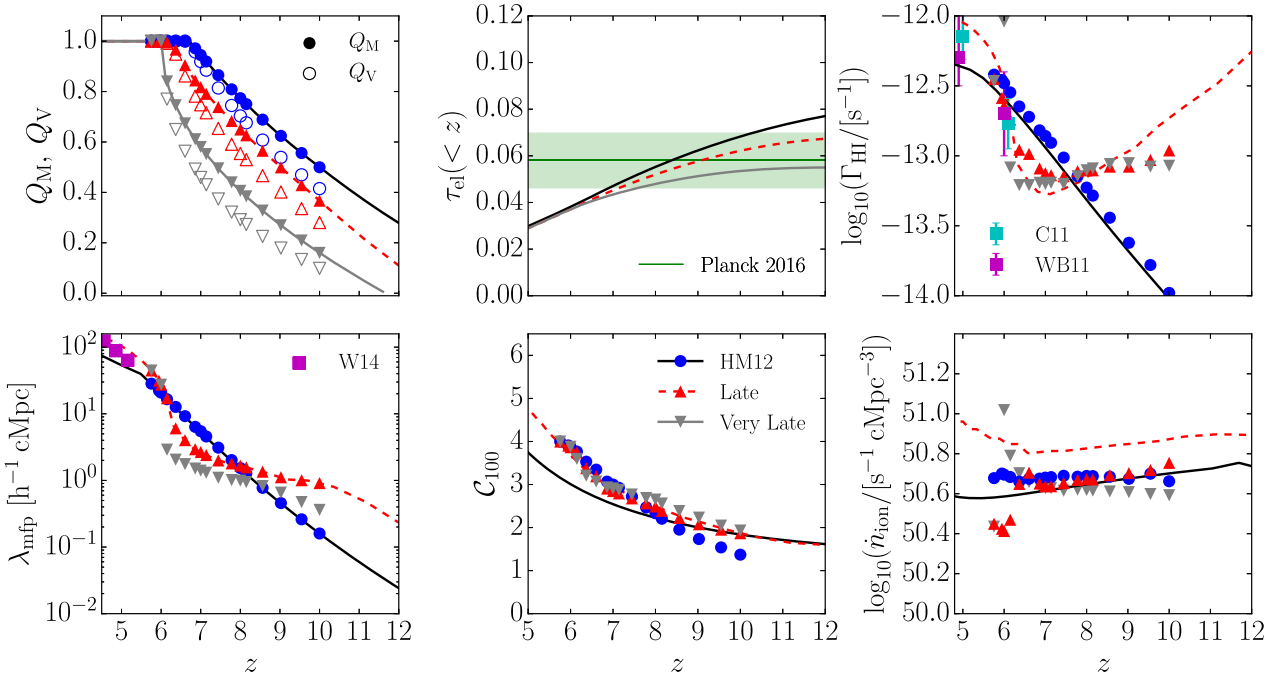

Figure 4. Calibrated parameters of the simulation. Clockwise from the top left: mass- and volume-averaged neutral fractions, electron-scattering optical depth, UV background photoionization rate, ionizing emissivity, clumping factor for overdensities less than 100, and ionizing photon mean free path within ionized regions. Our chosen models are shown as blue dots (HM12), red triangles (Late), and grey inverted triangles (Very Late). The reionization histories are shown as solid black (HM12 Haardt & Madau 2012) and red dashed (Ch15 Chardin et al. 2015) lines. Observed data from Calverley et al. (2011, C11), Wyithe & Bolton (2011, WB11), and Worseck et al. (2014, W14) are overplotted for comparison. Note that in the top middle panel (electron-scattering optical depth) we show the 1 σ bounds shaded in green from Planck Collaboration XLVII (2016).

of ionizing photons rises rapidly. For this more abrupt end to reionization to occur, there needs to be a sharper increase in the mean free path, which can be seen in the bottom left panel. We note that the recent physically motivated model of Puchwein et al. (2018) has been able to reproduce this required rather sharp increase.

4.2 Host halo masses

To model the effect of the IGM and the CGM on the Ly α emission, we have to simulate the underlying signal from the galaxies. This step of our simulation has two components: (i) the spatial distribution of galaxies in our simulation volume; (ii) the emission profile, $J(\nu)$, of the galaxies. We expect the galaxy spatial distribution to follow the halo distribution (Kaiser 1984; Verde et al. 2002). Unfortunately, the emission profile for high redshift galaxies is poorly constrained. Our modelling choices are motivated by the tests discussed in Section 3.3.

We consider three models for the spatial distribution of LAEs, based on different halo mass bins, choosing a sample of 4992 haloes per model. These models therefore have varying levels of correlation between the LAE positions and the positions/size of ionized regions.

(i) **Small mass**: First, we place the LAEs in haloes smaller than the mean mass, which on average have a mass $M_h \sim 10^9\,M_\odot/h$. This simple model is useful for understanding the evolution of faint LAEs.

(ii) **Large mass**: Secondly, we consider the case where LAE positions have maximal correlation with the ionized regions by placing them in the most massive haloes of the simulation volume. These haloes have masses in the range $10^{11} \lesssim M_h \lesssim 10^{12}\,M_\odot/h$. This model is used to represent the bright end of the LAE distribution.

(iii) **Continuous**: Finally, we place LAEs in a random sample taken from the full halo population of the simulation, noting that the mass resolution of the simulation naturally enforces a physically realistic cutoff mass $M_h > 10^7 M_\odot$ (Finlator et al. 2017). Due to the steep slope of the halo mass function, this model will be dominated by smaller more common haloes and hence will be similar in many respects to the small-mass model. It is intended as middle ground between the first two models, and we consider it the most realistic model for comparing with an observational survey of average LAEs.[7]

The first two models are used as approximate representations of the different populations of faint (lower mass host haloes) and bright (higher mass host haloes) LAEs.

In Fig. 5, we show the median velocity for the gas distribution along sightlines through the small-mass (cyan lines) and large-mass (magenta lines) haloes. The figure shows much larger infalling velocities around the large-mass haloes. Comparing across the different redshifts (with $z = 10$ represented by the dash–dotted lines, up to $z = 6$ represented by the solid lines), we also see more significant evolution in the larger mass haloes than for the smaller mass haloes. This evolution is largely driven by the evolution in the halo masses of our large-mass model, which can be seen in Table 1. Therefore, our large-mass model represents an upper limit on the possible con-

[7] Although we do not need to explicitly specify a mass-luminosity mapping for the results in this work, we note that for the commonly assumed linear relation of Ly α luminosity and host halo mass, $L_{Ly\,\alpha} \sim M_h$, the continuous model would correspond to a random sampling of the faint end of the luminosity function.

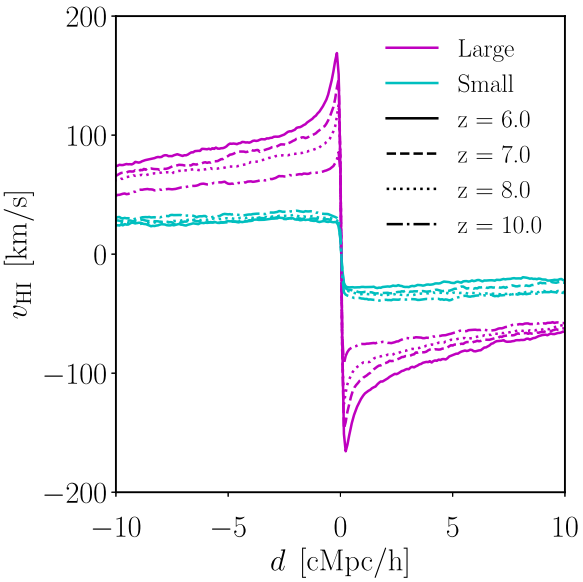

Figure 5. Median values of the hydrogen peculiar velocity around haloes (at $d = 0$ [cMpc h^{-1}]) are shown for the small-mass range (cyan) and large-mass range (magenta) for 5000 sightlines at $z = 6$ (solid), $z = 7$ (dashed), $z = 8$ (dotted), and $z = 10$ (dash–dotted). See Appendix A for a comparison of these simulation profiles with an analytical (excursion set) model.

Table 1. Averages masses of the different halo mass models used in this work.

Name	$\log_{10}(\overline{M}_{\rm h}$ [M$_\odot$])			
	$z = 6$	$z = 7$	$z = 8$	$z = 10$
Small mass	9.393	9.358	9.328	9.283
Large mass	11.531	11.259	11.002	10.518
Continuous	9.594	9.512	9.477	9.370

tribution the local gas environment evolution can provide towards Ly α attenuation.

We note that the peculiar velocities tend to zero with increasing radius but only on large scales of order 80 cMpc h^{-1}. As a result of the long-range correlations of peculiar velocities, out to large radii from the host halo, the gas is infalling with respect to the halo. Comparing to the neutral gas density profiles in Fig. 2, we see that the high-column density gas around the more massive haloes will be moved towards line centre (in the gas rest frame) by the large infalling velocities. Comparing these velocity profiles to the transmission curves in Fig. 3 suggests that there can be increased attenuation due to damping wing absorption by the neutral (self-shielded) gas around massive haloes compared to the less massive haloes of the small mass model.

For the second component of our source model, we assume a Gaussian emission profile, with centre offset (in the galaxy rest frame) from Ly α by a shift $\Delta\nu = \nu_\alpha \Delta v_{\rm int}/c$ and width given by $\sigma_\nu = \nu_\alpha \sigma_v/c$. Importantly, we account for the peculiar velocity of the emitter when using the emission profile for calculations in the frame of the sightline. The radiative transfer through the ISM produces a characteristic double-peaked emission profile (Dijkstra 2014); however, the blue peak will redshift into resonance while the photons traverse the IGM. At the considered redshifts, even residual neutral gas in ionized regions is sufficient to render this blue peak unobservable, hence our use of a singly peaked Gaussian emission profile. It has been empirically established that the Ly α emission line centre is offset in both high redshift LAEs and lower redshift analogues (Erb et al. 2014; Stark et al. 2015). A suggested

Table 2. Estimated average host halo masses at $z = 6.6$, using clustering statistics like the angular correlation function.

Work	$\log_{10}(\overline{M}_{\rm h}$ /[M$_\odot$])
Ouchi et al. (2010)	10–11
Sobacchi & Mesinger (2015)	$\lesssim 10$
Ouchi et al. (2018)	$10.8^{+0.3}_{-0.5}$

explanation for the cause of this offset is galactic outflows (Steidel et al. 2010; Shibuya et al. 2014) but almost certainly in combination with resonant scattering effects (e.g. Barnes et al. 2011). We use the same values of $\Delta v_{\rm int}$ and σ_v that were employed as the default model of CPBH15. The emission profile is the same for all the haloes, with $(\Delta v_{\rm int}, \sigma_v) = (100, 88)$ km s^{-1}. These values are similar to those inferred in Stark et al. (2015) using the C III]λ1909 line.

In summary, we have nine model permutations, which include the three reionization histories and the three halo mass models. Our fiducial model for comparison with observational data is the 'Late' reionization history combined with the continuous mass model. In Appendix B, we test further model variations, including changes to the emission model (such as mass and redshift-dependent velocity offsets).

4.3 Observational constraints on host halo masses from LAE clustering

The best constraint on host halo masses of LAEs can be obtained using clustering statistics. The estimates for $z = 6.6$ LAEs from Ouchi et al. (2010); Sobacchi & Mesinger (2015); and Ouchi et al. (2018) are shown in Table 2. The average masses of host haloes have been calculated in the above works using samples that span the luminosity range from faint ($10^{42} \lesssim L_{{\rm Ly}\,\alpha} < 10^{43}$ erg s^{-1}) to bright ($L_{{\rm Ly}\,\alpha} \gtrsim 10^{43}$ erg s^{-1}) and so do not necessarily reflect the expected masses for this distinction but rather an average of the two ranges. We leave it to future work to perform a detailed clustering analysis on the observed samples of LAEs split into these luminosity brackets. For comparison with this work, the average host halo masses at representative redshifts for our small- and large-mass models are shown in Table 1.

Note again the definition of our mass models: large corresponds to the most massive haloes in the simulation, which evolves with redshift; small corresponds to the most common haloes with mass $\sim 10^9$ M$_\odot$. A comparison of Tables 2 and 1 shows that the observed masses lie somewhere in between our small- and large-mass models. As mentioned in Section 4.2, our continuous model should thus be the most representative of a real LAE sample. Although the steepness of the halo mass function biases the average mass towards the smaller mass end of the spectrum, we still expect there to be LAEs hosted by the more massive haloes considered here.

5 RESULTS

Having applied our calibration scheme for the different reionization history models, and then calculated the Ly α transmission for the different LAE models, we can now explore the effect of these different model parameters on the distribution of transmission fractions. We can also explore the effect on the TFR (transmission fraction ratio, as defined in Section 3.4) evolution and compare this to the observed difference between bright and faint LAEs. Finally, we can also derive the evolution of the Ly α fraction, $X_{{\rm Ly}\,\alpha}$, and compare our predictions with observations.

5.1 Evolution of the median transmission

In Fig. 6, we show the attenuation effect of the IGM on the initial galactic emission profile. The top panel shows the components involved in the transmission fraction calculation: the emission profile in dashed green, the transmission in solid shades of purple (with shade darkening as redshift increases, for the small-mass model), and the resulting transmitted emission profile (after IGM reprocessing) in solid shades of green.

The transmission fraction is given by the area under this reprocessed emission profile, as discussed in Section 3.1. The lower set of panels show the reprocessed emission profile for six of the model combinations: the reionization histories from top to bottom and the small- and large-mass models in the left and middle panels, respectively. We also show three further model combinations in the right-hand panels, in which the large-mass model is paired with a larger intrinsic velocity offset of $300\,\mathrm{km\,s^{-1}}$ than our default $100\,\mathrm{km\,s^{-1}}$. In general, the presence of neutral hydrogen gas during the EoR causes the peak of the emission profile to be translated redwards in frequency space and to be reduced in amplitude. We note that the evolution of the profile is most rapid in the Very Late model. For each reionization history, it also occurs more rapidly for the small-mass model. The trend for the frequency translation of the profile with redshift is different between the small and large models. The small model profile reddens with increasing redshift. In the large-mass model, the shift in frequency is less clear. We see that for the same intrinsic emission profile, the resulting profile is more strongly attenuated for the large-mass haloes at a given redshift. In the right-hand panels where we have used a larger intrinsic velocity offset ($\Delta v_{\rm int} = 300\,\mathrm{km\,s^{-1}}$), we see that instead the large-mass halo profiles are less (or equivalently) attenuated compared to the small-mass profiles. This demonstrates that the IGM and CGM attenuation of the Ly α luminosity is indeed very sensitive to the intrinsic emission profile. Despite this significant effect seen when comparing at a given redshift, we find that the relative transmission evolution (i.e. normalized to a given reference redshift, as described in Section 3.4) is less sensitive to the intrinsic emission profile. For further details, see Appendix B.

5.2 Transmission fraction distribution

We apply the framework from Section 3.1 (equation 15) to explore the difference in the distributions of the transmission fractions for the small- and large-mass models. In Fig. 7, we show the (normalized) probability distribution for the transmission fraction at $z = 7$; we show the small-mass (black line) and large-mass (red line) models (as well as a large-mass model with increased velocity offset of $300\,\mathrm{km\,s^{-1}}$ shown with the dotted red line). Considering first the small-mass model distribution in black, we see a bimodal distribution with peaks around $T \sim 0$ and $T \sim 0.6$. The $T \sim 0.6$ peak can be understood as those sightlines that start in host haloes sitting in ionized regions, where there is no sufficient recombined neutral hydrogen (or the neutral gas is not infalling with a high-enough velocity) to completely reduce the transmission fraction in the ionized region. The photons emitted in the vicinity of such haloes can redshift beyond the damping wing by the time they reach the edge of the ionized region and hence will be transmitted along the sightline. The dominant $T \sim 0$ peak is due to sightlines where photons emitted at the halo position would be absorbed/scattered somewhere along the sightline. This absorption might be due to self-shielded clumps, recombined hydrogen in the ionized regions, or residual neutral hydrogen in the rest of the IGM. Comparing this to the large-mass model distribution in solid red, we see instead a single peak around $T \sim 0$, although there is also a small non-zero probability of $T > 0.8$ which was not present in the small-mass model distribution. Finally, the red-dotted line shows the same large-mass model but using a larger intrinsic velocity offset of $\Delta v_{\rm int} = 300\,\mathrm{km\,s^{-1}}$ (compared to the default of $100\,\mathrm{km\,s^{-1}}$). This distribution now recovers a second peak at $T \sim 1$. We note that the mean transmission fraction is higher for the sightlines that start on the small-mass haloes, unless the larger velocity offset is used for the large-mass model haloes.

These distributions may seem counterintuitive, as the more massive haloes should sit in larger ionized regions and hence be more visible on average. This picture, however, does not take into account the infalling velocities of the neutral gas within ionized bubbles, either recombined or self-shielded, which are considerably larger for the more massive haloes (as seen in Fig. 5). This infall towards the halo counteracts the cosmological redshifting of the emitted photons such that they are closer to line centre in the frame of the gas, which leads to greater absorption (unless the intrinsic offset is increased). The $T \sim 1$ peak in the default large-mass model (red solid line) is diminished because although these emitters sit in large ionized regions, the self-shielded gas within the ionized region can still strongly attenuate the Ly α emission. However, when the intrinsic offset is increased, such that this self-shielded gas becomes more transparent to Ly α radiation, we recover the peak we would expect close to $T \sim 1$.

In this way, we see that at a given redshift the presence of neutral CGM gas can lead to an increase in halo-to-halo scatter of the transmission in our mass samples. We note, however, that the average evolution of the transmission is driven by the neutral IGM. The relative importance of the CGM/IGM absorption in Ly α visibility will be explored further in Section 6.2.

5.3 Transmission fraction evolution in the small, continuous, and large-mass models

As discussed in Section 3.4, we can quantify the evolution of the transmission fraction by normalizing to a reference redshift value (here chosen to be $z = 5.756$), which we call the TFR. We calculate the mean TFRs at a given redshift for the three mass models in the three different reionization histories. This can be used to compare how the visibility of LAEs in the different mass models evolves. In Fig. 8, we plot the TFR evolution of the small-mass (cyan) and large-mass (magenta) models, with 1 σ scatter shown by the shading. We estimate this scatter by repeatedly sampling the transmission fraction distribution at each redshift, with sample sizes comparable to the observational sample sizes.[8] This results in an increase in scatter with redshift as the sample sizes decrease, reflecting the increase in statistical uncertainty. Beyond redshift $z = 7.3$, the sample size is kept constant, and the scatter starts to decrease as the halo-to-halo variation decreases (because at high redshifts the universe was more homogeneously neutral). In all reionization histories before percolation ($z \gtrsim 6$), we find that the large-mass model evolves considerably slower than the small-mass model. We see greater scatter in the large-mass model; this is likely because the large-mass model contains some rare very massive haloes, such that there is a non-negligible difference in environment between the most and least massive haloes within the large-mass model. This leads to more halo-to-halo variation in the Ly α transmission along

[8]We note that for their luminosity function samples, Konno et al. (2018) found 1081 LAEs at $z = 5.7$ and 189 at $z = 6.6$.

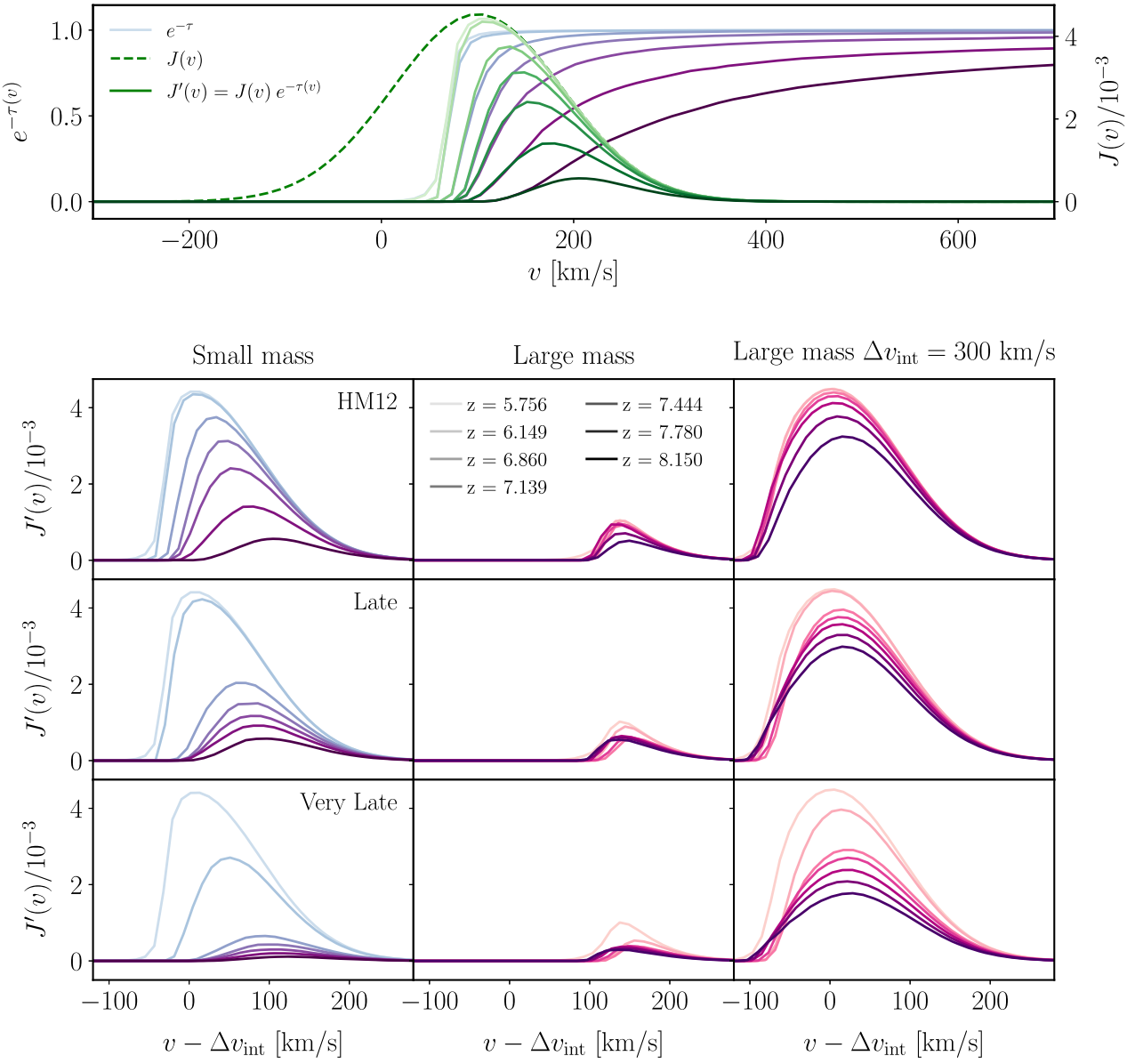

Figure 6. *Top panel*: The (normalized) initial emission profile $J(v)$ (assuming $\Delta v_{\rm int} = 100\,{\rm km\,s^{-1}}$, green dashed line) and the median transmission $e^{-\tau(v)}$ (purple solid lines) redward of line centre ($v = 0$), between $z = 5.756$ (light) and $z = 8.150$ (dark), are shown for the small-mass model. The resulting emission profiles (green solid lines) after IGM reprocessing are found as the overlap of these two curves, $J' = e^{-\tau} J$. *Bottom panels*: The resulting median emission profiles for the different mass and reionization history models. The small-mass host halo model is shown on the left and the large-mass model in the middle panels. The right-hand panels also show the large-mass results but found using a larger intrinsic velocity offset of $\Delta v_{\rm int} = 300\,{\rm km\,s^{-1}}$. The reionization histories (HM12, Late and Very Late) are shown from top to bottom.

these sightlines, compared to the small-mass model (whose mass bin width is smaller).

Overplotted on Fig. 8 for reference are a selection of observed TFRs reported by Zheng et al. (2017, Z17), Konno et al. (2018, K18), Konno et al. (2014, K14), Ota et al. (2017, Ot17), Itoh et al. (2018, It18), and Ouchi et al. (2010, Ou10), all normalized to $z = 5.7$. Importantly, the TFRs quoted by observers are usually calculated from a full (luminosity spanning) sample of LAEs, i.e. *including* both bright and faint LAEs. As the small- and large-mass models represent extreme examples of LAEs, the most meaningful comparison with observational data is with our continuous model. Nonetheless, we overplot the observational data on all TFR figures, in order to give a reference point for comparison.

In the rightmost panel of Fig. 8, we show the evolution of the TFRs for the continuous model, with the different reionizaton histories represented by different colours. We note that the 'Late' (in red) and 'Very Late' (in grey) reionization histories are the best matches to the observed data, suggesting a reionization history somewhere in between these two bracketing models. The scatter in the continuous model is comparable to the scatter in the small-mass model, which in turn is similar to the observational errors.

5.4 Differential evolution of the transmission fraction

Alongside the average TFRs reported by observers, some (e.g. Zheng et al. 2017) have also reported that the TFRs for bright

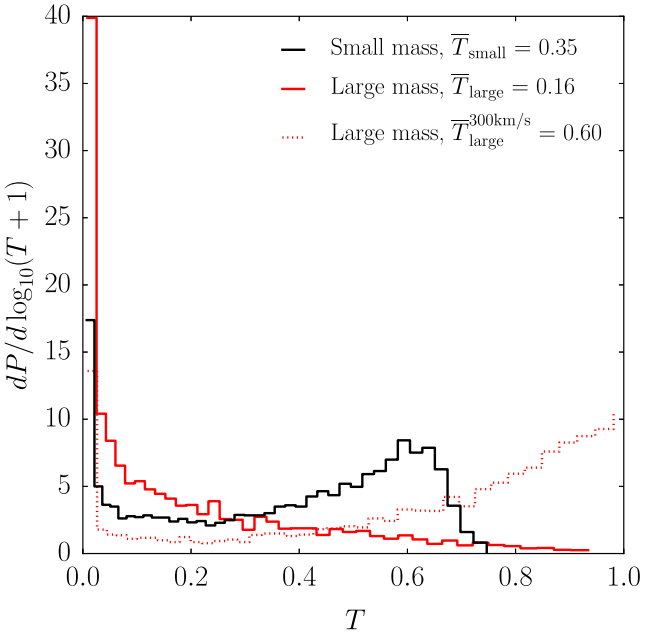

Figure 7. The distribution of transmission fractions for the small- (black) and large- (red) mass models at $z = 7$, using the fiducial Late reionization history. The red-dotted line shows the large-mass model distribution if the intrinsic offset is instead $\Delta v_{\rm int} = 300\,{\rm km\,s^{-1}}$.

LAEs are higher than for faint LAEs. This behaviour is reproduced by our large (representing bright LAEs) and small (representing faint LAEs) models, which show a difference in the TFRs for the same redshifts as seen in Fig. 8.

To compare this more explicitly, we use reported observational data from Konno et al. (2014); Zheng et al. (2017); Matthee et al. (2015); and Santos et al. (2016) to reconstruct the TFRs for the bright and faint LAEs separately. In this way, we want to establish trends and obtain a lower limit on the bracketing values for the TFRs and so do not perform a detailed re-analysis of the data. We take values of $\Phi(L) = {\rm d}n/{\rm dlog}_{10}L$ as quoted in the original works. From these, we calculate

$$\rho(z) = \int_{L_{\rm min}}^{L_{\rm max}} L\,\Phi(L)\,d\log_{10} L. \quad (28)$$

In order to perform this integral, we apply a trapezoidal algorithm on the published data points; we do not fit a Schechter form. The data are heterogeneous in terms of the luminosity ranges observed, so we impose limits, $L_{{\rm Ly}\,\alpha} \in [42.5, 43.7]$ erg s^{-1}, and use linear interpolation and extrapolation to evaluate each of the data sets in the same luminosity bins along this range. There is obviously freedom in the choice of the 'bright' threshold; we test values around $\log_{10} L^{\rm bright}_{\rm min} = 43$, bracketing $\log_{10} L^{\rm bright}_{\rm min} = 43.4$ as used in Zheng et al. (2017). The threshold used for the calculated values plotted in Fig. 9 is $\log_{10}(L^{\rm bright}_{\rm min}/{\rm erg\,s^{-1}}) = 43.1,\ 43.3,\ 43.5$. We then calculate the TFRs using the expression in equation (24), with the UV data from Finkelstein et al. (2015),[9] assuming $\kappa(z = 5.7)/\kappa(z = 6.6) = 1$ and $f_{{\rm esc,\,Ly}\,\alpha}(z = 5.7)/f_{{\rm esc,\,Ly}\,\alpha}(6.6) = 1$.

The green markers in Fig. 9 show the (re-calculated) difference in the TFRs for the bright and faint LAEs, compared to the simulated differences between the large- and small-mass models (lines coloured by reionization history). The differential TFR evolution depends on the chosen reionization history, but the shape of this evolution is similar across the models. We will discuss this further in Section 6.1. Note that changing the bright threshold in the observed data alters the amplitude of the difference and the slope across redshifts.[10]

5.5 Evolution of the Ly α fraction of LBGs

Finally, we also consider the independent observational measurement of the Ly α fraction of LBGs, $X_{{\rm Ly}\,\alpha}$, to see if our large- and small-mass models can be used to reproduce the UV bright and UV faint evolution. We calculate this evolution as described in Section 3.5.

In Fig. 10, we compare the evolution of $X_{{\rm Ly}\,\alpha}$ predicted by our simulations with the observed data for the thresholds of $\mathcal{W} > 25$ Å and $\mathcal{W} > 55$ Å. Our models are again reasonably consistent with the data; the largest discrepancy is found for the steep drop in the $\mathcal{W} > 25$ Å UV faint data of Stark et al. (2011), which only our 'Very Late' model is able to reproduce. We note that the use of the large-mass model for the UV bright data accounts for the slower decline in this sample, whilst the faster evolution of our small-mass model is a good fit for the UV faint sample. Apart from the left-hand panel ($\mathcal{W} > 55$ Å UV faint), the comparison with observational data does not exclude any of our reionization history models.

Comparing with SZM17 (Sadoun et al. 2017), we see similar predictions to their infall model, despite having a more modest evolution of $\Gamma_{\rm HI}$[11] in our simulations.

6 DISCUSSION

In Section 5.4, we have shown that our simulations predict a difference in the evolution of the visibility of LAEs hosted in different mass haloes. If we assume that indeed brighter LAEs are found in more massive host haloes, then this can explain the different evolution of bright and faint high-redshift LAEs. We now discuss possible physical mechanisms for this difference in our simulations. We caution, however, that some of the observed difference could also be due to observational selection effects.

6.1 Differential evolution of large- and small-mass models

Neglecting intrinsic galaxy evolution, we explore here two different aspects of the IGM and CGM attenuation that might cause the different evolution of the bright and faint LAE populations.

(i) The most intuitive mechanism is perhaps the different (large-scale) environments of ionized bubbles in which LAEs might reside (for example, suggested by Ota et al. 2017, in Section 4.1). More massive haloes are likely to reside in larger ionized regions compared to less massive haloes. In particular, we might also expect that (depending on the reionization history) more massive haloes

[9] We also calculated using UV data of Bouwens et al. (2015), but the bright/faint trend persists regardless of this change.

[10] We note that the simulated TFR difference is sensitive to the chosen mass bins, and hence without better constraints on host halo masses, the observed TFR differences cannot be used to constrain the most likely reionization history. Our large- and small-mass models are nevertheless useful for demonstrating that a difference does indeed occur.

[11] Their model considers a change between $z = 7 \rightarrow 6$ in the photoionization rate of $\Gamma_{\rm HI} = 10^{-14} \rightarrow 10^{-13}\,{\rm s^{-1}}$; the minimum $\Gamma_{\rm HI}$ in our models between $6 < z < 8$ does not fall below $10^{-13.2}\,{\rm s^{-1}}$.

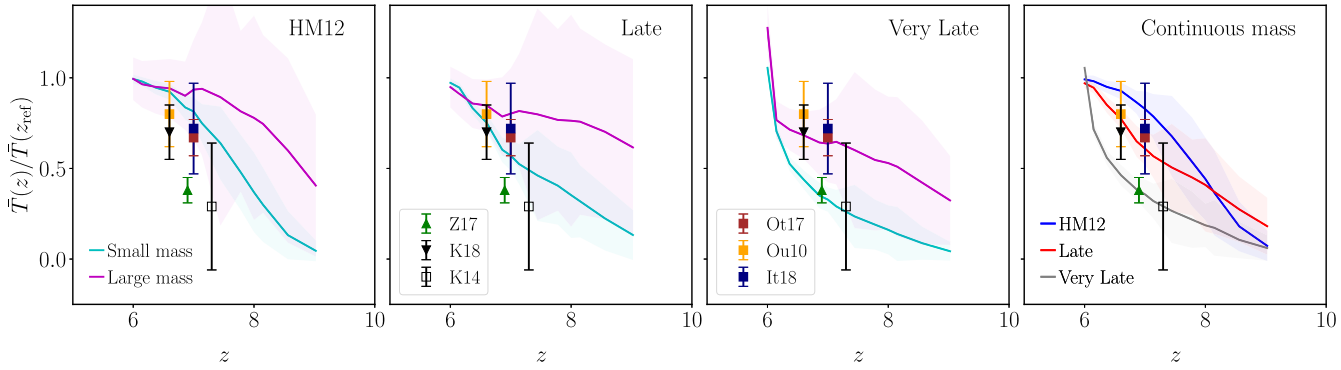

Figure 8. Evolution of the mean transmission fractions (TFRs), normalized to $z_{\rm ref} = 5.756$. *Left-hand three panels*: The large- (magenta) and small- (cyan) mass models are shown in all panels. The shaded regions show the 68 per cent scatter in the TFR values found by sampling the distribution with sample sizes comparable to observational LAE samples at each redshift. From left to right, we have the different reionization histories: HM12, Late and Very Late. Overplotted are data from Zheng et al. (2017, Z17), Konno et al. (2018, K18), Konno et al. (2014, K14), Ota et al. (2017, Ot17), Itoh et al. (2018, It18), and Ouchi et al. (2010, Ou10) normalized to $z_{\rm ref} = 5.7$, where errors were not quoted in these works we have made a basic estimate. Note that these observational data points were found by considering the luminosity density across the faint ($42 \lesssim \log_{10} L_{{\rm Ly}\,\alpha} \lesssim 43$) and bright ($\log_{10} L_{{\rm Ly}\,\alpha} \gtrsim 43$) ends of the luminosity functions. Therefore, these observational points are best compared to the continuous model, as shown in the rightmost panel. *Rightmost panel*: The TFR evolution of the continuous mass model. The different reionization history models are shown in blue, red, and grey, with the corresponding shading indicating 1σ scatter. This model represents a middle ground between the extreme small- and large-mass models. Note that in all these panels, the emission profile was our default model with $\Delta v_{\rm int} = 100\,{\rm km\,s^{-1}}$.

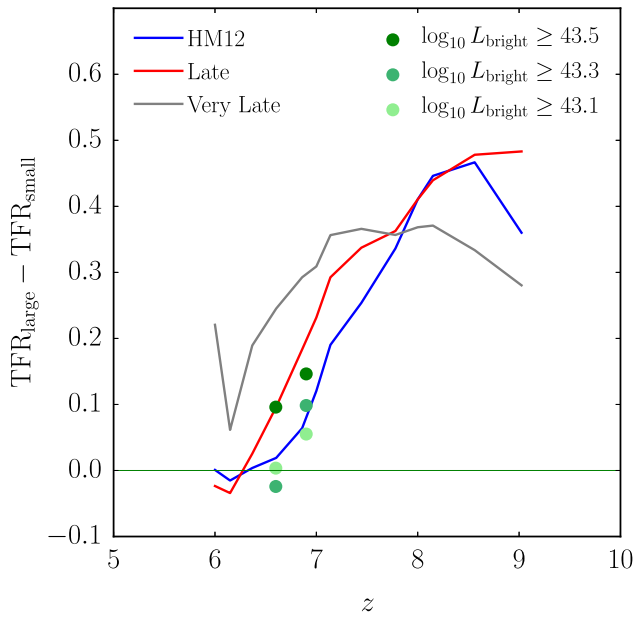

Figure 9. Difference in the evolution of the TFRs (normalized to $z_{\rm ref} = 5.756$) between the large- and small-mass models. Overplotted in shades of green are observed differences, derived with data from Konno et al. (2014); Zheng et al. (2017); Matthee et al. (2015); and Santos et al. (2016) (these data were also normalized to $z_{\rm ref} = 5.7$). Three different brightness thresholds are shown: $\log_{10}(L_{\rm min}^{\rm bright}/{\rm erg\,s^{-1}}) = 43.5,\ 43.3,\ 43.1$. Note again that in all these models, the emission profile was our default model with $\Delta v_{\rm int} = 100\,{\rm km\,s^{-1}}$.

will be surrounded by ionized regions earlier, after which their visibility will not evolve dramatically; in comparison, the less massive haloes will enter overlapping ionized regions around the more massive haloes at later times.

(ii) A second, more subtle mechanism is due to the different dynamical properties of neutral hydrogen in the CGM. In Fig. 5, we showed the evolution of the infall velocity of gas around haloes of different masses. We might expect both the gas close to the halo (which includes self-shielded or recombined neutral hydrogen within the ionized region) and the residual neutral gas in the not-yet-ionized IGM around the halo to absorb differently depending on the host halo mass.

In order to explore the contributions of these two mechanisms in our models, we perform the following two tests.

(i) *Spatial correlations with ionized bubbles*: We displace the ionization field along one direction of the simulation by a distance $d = 80$ cMpc $\rm h^{-1}$, half the simulation box length. This will break the correlation between the location of haloes and ionized regions. If the higher TFRs of the more massive host haloes are caused by their position in larger ionized bubbles, then this test should result in the TFRs of the small-mass and large-mass models converging.

(ii) *CGM peculiar velocities and temperature*: We re-calculate the optical depths along the extracted sightlines but neglect both the peculiar velocities and the temperature variation of the CGM.

Note, however, that the two mechanisms are coupled and that the two tests are therefore not independent of each other. In particular, in the first test by displacing the ionization field, we will also be removing some of the correlation between the infalling velocities of neutral gas and the haloes. We should therefore not expect the two tests to quantify how much each of the mechanisms is contributing to the difference in TFR evolution, but they should nevertheless show whether these two mechanisms are indeed having an effect.

In Fig. 11, we plot the difference between the TFRs for the large- and small-mass models as a function of redshift. The left-hand panel shows the spatial correlation test. The difference drops close to zero for all reionization histories, suggesting that indeed the difference of the visibility of smaller and larger mass haloes decreases significantly if there is no correlation of their location with that of ionized bubbles. We note that the effect of the correlation depends on the reionization history. The strongest effect of removing the correlation is seen in the Very Late model and it is weakest for the HM12 model.

This can be understood by considering the rate with which smaller haloes enter the large-scale overlapping ionized regions. The over-

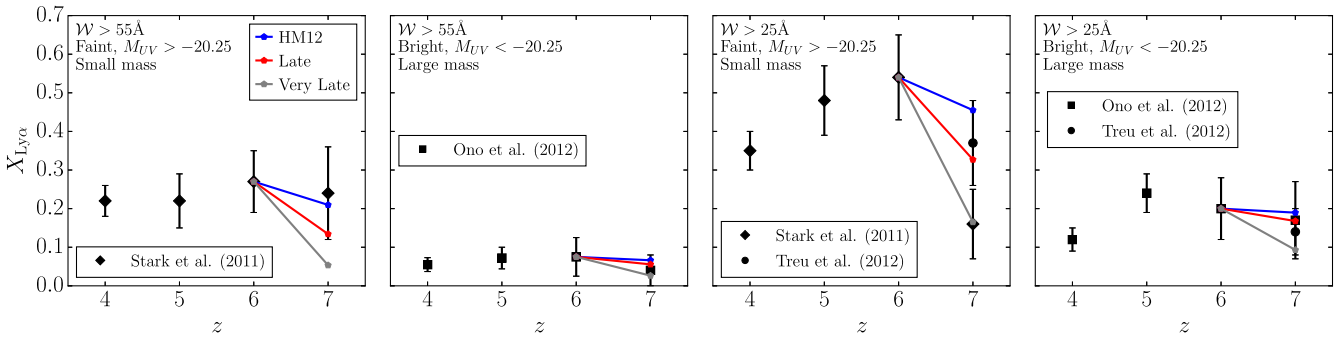

Figure 10. The fraction of galaxies emitting Ly α above a given threshold equivalent width $\mathcal{W}$ (EW), as a function of redshift. These distributions were calculated using the small-mass model (first and third panels, UV faint) and large-mass model (second and fourth panels, UV bright). The different reionization models are shown as blue (HM12), red (Late), and grey (Very Late) lines. For comparison, the observed *UV faint* ($M_{\rm UV} > -20.25$) data from Stark et al. (2011, diamonds) and Treu et al. (2012, circles) and *UV bright* ($M_{\rm UV} < -20.25$) data from Ono et al. (2012, squares) and Treu et al. (2012, circles) are also shown.

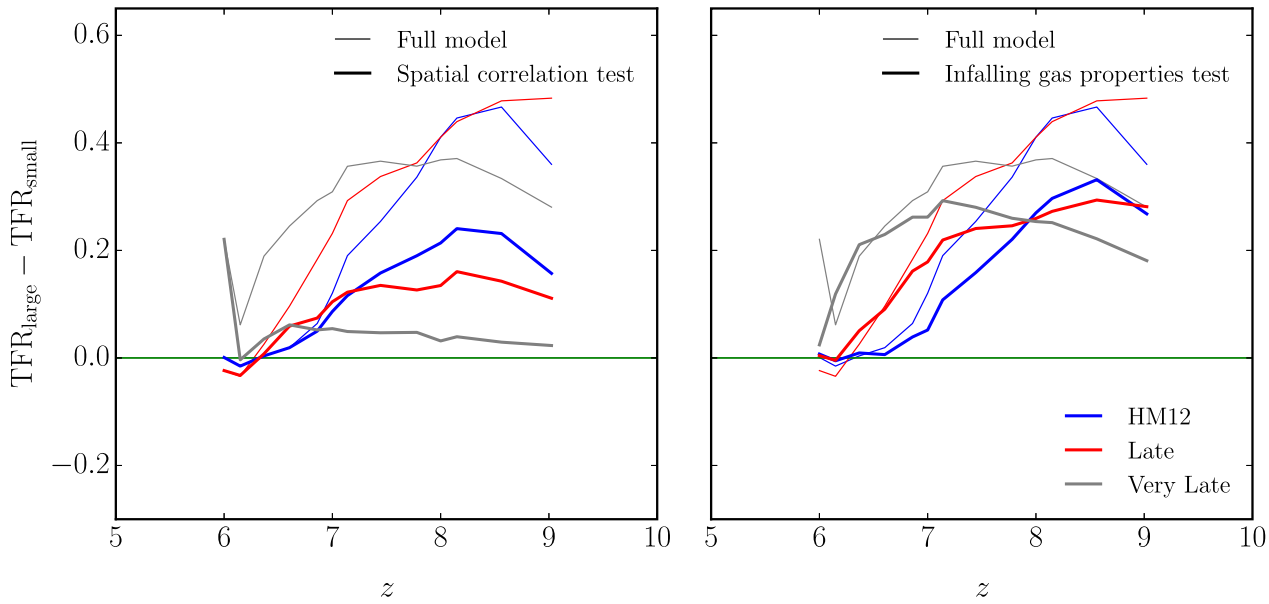

Figure 11. Evolution of the ratio of transmission fractions, testing the effect of the CGM/IGM on the differential visibility of large and small host haloes. The difference in TFR between the large- and small-mass models is plotted for the full models (thin lines) and the test cases (thick lines). In the left-hand panel, we show the 'Spatial correlation test', whilst in the right-hand panel, we show the 'Infalling gas properties test'. The different reionization history models are shown in blue (HM12), red (Late), and grey (Very Late).

lapping ionized regions initially develop around the largest haloes that provide a bigger fraction of the total ionizing photon budget, and hence these haloes remain in ionized regions out to higher redshifts. Smaller haloes enter into these ionized regions later, when the ionization fronts around the larger haloes percolate and expand into the ionization fronts around these smaller haloes. How quickly the smaller haloes enter the ionized regions depends strongly on the reionization history, both on $Q_{\rm M}(z)$ and $dQ_{\rm M}/dz(z)$. In the HM12 model reionization ends early such that around $z \sim 7$ both the small and large halo positions are strongly correlated with the ionized regions. This means that the difference in visibility of these haloes is mostly not determined by the sizes of the ionized bubble. In the Very Late model, in which reionization ends later and more rapidly, there is a much larger difference in the bubble sizes surrounding the small and large haloes at $z \sim 7$.

In the right-hand panel of Fig. 11 we show the effect of neglecting gas peculiar velocities and temperatures of the CGM surrounding the host haloes. Neglecting these gas properties, there will be less absorption in neutral hydrogen around the host halo (both within reionized regions and also in the residually neutral IGM). For this test, there is also a dependence on the reionization history; however, for all our reionization models, the effect is less significant than that of removing the spatial correlation with the ionized bubbles. The influence of the infalling gas properties increases with redshift. For example, the fractional difference from the full calculation in the Late model is ∼0.3 at $z = 8$ but rises to ∼0.4 by $z = 9$.

In summary, the results of our two tests suggest that dependent on the reionization history ,

(i) the positions of more massive haloes in larger ionized regions can make a significant contribution to the differential visibility of the large- and small-mass models; and

(ii) the infalling gas properties of neutral IGM gas also play a, albeit smaller, role in the increased visibility of the large-mass model.

We also note that the largest difference in visibility occurs for the Late reionization history.

6.2 The effect of self-shielding and the dominant scales on which IGM attenuation occurs

In SZM17 (and also in earlier work such as Dijkstra, Lidz & Wyithe 2007; Kakiichi et al. 2016), the role that the infalling CGM gas plays in the Ly α attenuation was explored. We have seen in Fig. 3 that the self-shielded gas in the CGM can indeed attenuate Ly α alongside the more distant neutral gas in the not yet ionized regions of the IGM. The strength of the attenuation depends on the amount of self-shielded gas present and hence also on the local photoionization rate. As the global neutral fraction of the large-scale IGM is also coupled to the photoionization rate, we note that these two attenuating components are also coupled. Within our models, the strength of the attenuation due to the self-shielded gas in the CGM will depend on the assumed self-shielding prescription, the amount of gas that is excluded from within the host halo, and the intrinsic velocity offset of the Ly α-emission profile. In this subsection, we aim to explore the interplay between this inner CGM self-shielded gas and the external (residual) neutral IGM gas to try to quantify the strength of the roles that they play in attenuating Ly α from high redshift galaxies.

In Fig. 12, we show how the transmission fraction at $z = 6$ depends on the background photoionization rate. In all of our reionization histories at this redshift, the IGM is ionized ($Q_{\rm M} = 1$), and so only the self-shielded/recombined CGM gas can play a role. In order to quantify how strong the attenuation can be from this gas, we normalize the transmission fraction to the value for $\Gamma_{\rm HI} = 10^{-12}$ s^{-1}. In each of the three panels of Fig. 12, we then test the effects of our assumptions: on the left the self-shielding prescription, in the middle the exclusion regime, and on the right the emission profile offset. In all panels, we see that decreasing the background photoionization rate (and therefore increasing the amount of self-shielded gas) increases the attenuation of Ly α. We note that in our fiducial reionization history, however, the background photoionization rate does not fall lower than $\Gamma_{\rm HI} \sim 10^{-13.2}$ s^{-1}.

In this work, we have employed the self-shielding prescription suggested by Chardin et al. (2018) (labelled SS-Ch). Other works have used different prescriptions for self-shielding, which can lead to more neutral gas and thus a stronger attenuation of Ly α emission. In the left-hand panel of Fig. 12, we compare our fiducial prescription with (i) the case of no self-shielding, and (ii) with a prescription based on Rahmati et al. (2013) (the default choice of CPBH15, labelled SS-R). As expected, we see that the stronger the self-shielding, the more attenuation can come from this CGM gas. However, even in the case of no self-shielding, where the amount of neutral gas is given only by recombinations in photoionization equilibrium, we see that if the photoionization drops sufficiently, then the transmission fraction can be reduced. In the middle panel, we see the effect of excluding different amounts of the CGM gas. Importantly, we note that for our default SS-Ch self-shielding prescription and photoionization rates larger than $\Gamma_{\rm HI} \sim 10^{-13}$ s^{-1} (that are suggested by full radiative transfer simulations of reionization), the attenuation is not very sensitive to the size of the exclusion region. In the right-hand panel, we show the effect of changing the intrinsic velocity offset of the emission profile. We see that of the three assumptions tested in this figure, the results are least sensitive to this choice.

Note that for the photoionization rates in our reionization histories, the self-shielded CGM gas alone can attenuate the Ly α signal by as much as $\sim$30 per cent for the Rahmati et al. (2013) self-shielding. For this model, the dependence on the size of the exclusion region is therefore also stronger than our default self-shielding model.

In order to explore this further, we also show the effect of changing our assumptions for the full TFR evolution in Fig. 13, using the continuous mass model and the Late reionization history. This therefore includes the contributions of both the CGM and the IGM. As in the previous figure, on the left-hand panel we show the effect of the self-shielding prescription, in the middle we show the effect of the exclusion region, and in the right-hand panel, we show the effect of the velocity offset. In the left-hand panel, we also include the prescription used in Bolton & Haehnelt (2013) (labelled SS), which assumes a sharp threshold for self-shielding at the Jeans scale. The results found without self-shielding can be considered as the attenuation due to the residual neutral IGM alone. We see that the neutral IGM is the dominant component in determining the average redshift dependence of the attenuation. However, the self-shielded gas can also play an important role, depending on the self-shielding prescription (SS resulting in the most self-shielding, and SS-Ch the least). In the central panel, we see the effect of excluding different amounts of the CGM gas. For exclusion regions $>2R_{\rm vir}$, the TFR depends very weakly on the exact choice of exclusion radius and values close to those in the No-SS case (shown in the left-hand panel) are found. Finally, we see in the right-hand panel that varying the intrinsic velocity offset does not alter the TFR evolution very much. Although the transmission at a given redshift might be sensitive to these changes, the normalization of the TFR removes part of this sensitivity (so long as the velocity offset is independent of redshift).

6.3 Observational selection effects

Throughout this work we have relied on the basic assumption that there is a positive correlation between the host halo mass and a galaxy's (rest frame) Ly α luminosity. Ly α photons are created in a galaxy's ISM by reprocessing the ionizing photons emitted from the stellar component. The Ly α luminosity depends on the SFR, which in turn depends on the host halo mass, $M_{\rm h}$ (Zheng et al. 2010). Given the often bursty nature of star formation, it is nonetheless not obvious that the brightest LAEs are hosted in the most massive haloes.

In the first instance, we have calculated the TFR evolution and compared to narrow-band Ly α-selected galaxies (such as in Ouchi et al. 2010). We split the samples into *bright* and *faint* based on the observed Ly α luminosity. For this selection method, a galaxy might be categorized as a bright LAE but might not necessarily be hosted by a more massive host halo. This is because the flux in the Ly α narrow-band filter is compared with a (sometimes overlapping) broad-band filter; the galaxy may appear bright with this selection method because there is more flux in the narrow-band than in the UV continuum. This therefore includes cases where the UV continuum is faint, and hence the galaxy may be less massive.

We have also calculated the evolution of $X_{{\rm Ly}\,\alpha}$ and compared to dropout-selected galaxies with spectroscopically confirmed Ly α equivalent widths ($\mathcal{W}$) above a given threshold (such as in Ono et al. 2012). These galaxies are first selected using the Lyman break technique and divided into UV bright and UV faint, based on bolometric UV luminosity. This UV luminosity correlates with stellar mass, and hence the UV-brighter objects will be hosted in larger mass haloes. The secondary Ly α-equivalent width selection does not change this measurement, so in this case the brighter LAEs

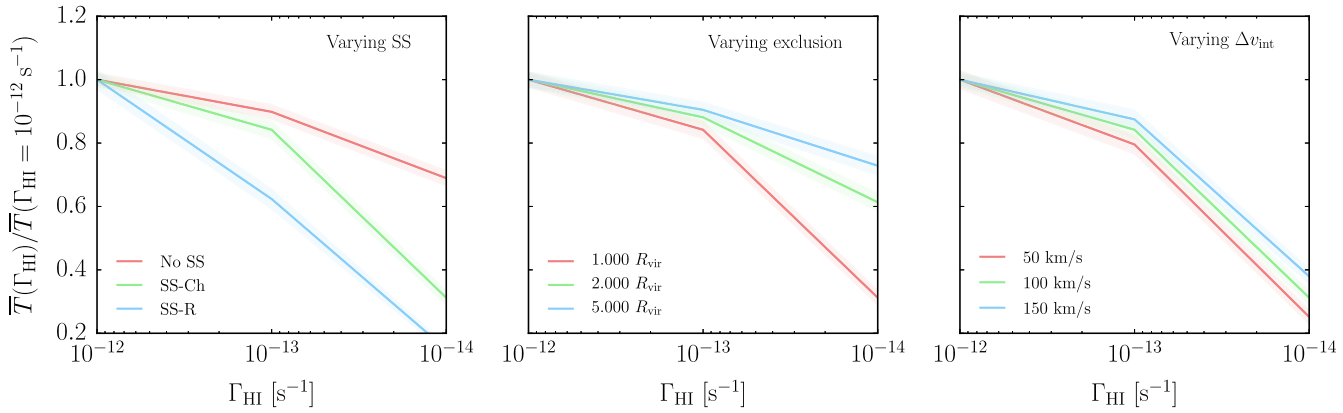

Figure 12. The photoionization rate dependence of the transmission fraction at $z = 6$ normalized to the value when $\Gamma_{\rm HI} = 10^{-12}$ s^{-1}. *Left*: The effect of varying the self-shielding prescription. *Middle*: The effect of varying the amount of gas that is excluded around the halo position. *Right*: The effect of varying the intrinsic velocity offset of the emission profile. Shading indicates 68 per cent scatter around the mean, calculated as in Fig. 8.

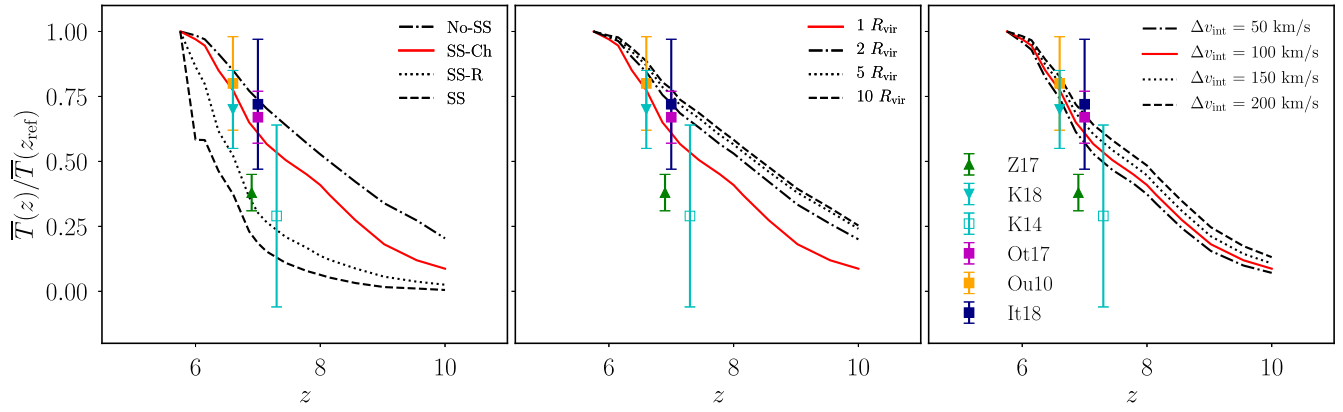

Figure 13. Testing the effects of different assumptions on the TFR evolution. *Left*: The effect of a range of self-shielding prescriptions, using the Late reionization history and the continuous model. The fiducial prescription used in this work is the SS-Ch model based on Chardin et al. (2018), shown in red. *Middle*: The effect of excluding gas around the halo, within a number of virial radii. Our fiducial exclusion is 1 $R_{\rm vir}$, shown in red. We note that beyond an exclusion of two virial radii, the evolution is very insensitive to the exact choice of exclusion radius; however, there is still a strong attenuation. This remaining attenuation is due to the large-scale neutral IGM, as previously modelled. *Right*: The effect of changing the intrinsic velocity offset of the emission profile. Our fiducial offset is 100 km s^{-1}, shown in red. Overplotted are observed TFR values, as in Fig. 8.

will almost certainly correspond to more massive haloes. Dayal & Ferrara (2012) have suggested that indeed the $z > 6$ LAEs form a luminous subset of LBGs.

The applicability of our different mass models and, in particular, the mapping from these models to the different populations of LAEs (divided by brightness) is therefore dependent on the way the population is selected. The TFRs we have calculated using the continuous mass model are probably the most realistic. For the $X_{{\rm Ly}\,\alpha}$ evolution, however, our application of the different mass models to the different UV brightness samples is probably better justified.

7 CONCLUSIONS

We have updated the modelling of the rapid evolution of Ly α emitters by CPBH15 (Choudhury et al. 2015) using the high-dynamic-range Sherwood simulations as a basis for our analytical model for the growth of ionized regions. We have, in particular, assessed the effect of host halo mass on LAE visibility just before the percolation of H II regions occurs at $z \sim 6$. Our main results can be summarized as follows:

(i) Our simulations naturally reproduce the observed strong difference in the evolution of the visibility of bright and faint LAEs at $z \gtrsim 6$ if we assume that bright LAEs are placed in the most massive haloes in the simulations with similar space densities as observed for bright LAEs.

(ii) The less rapid evolution of the visibility of bright LAEs in our simulations at $z > 6$ is only partially due to their strong spatial correlation with the first regions to be reionized, an explanation that has been invoked by other authors. In our simulations, we find an additional contribution: the different gas peculiar/infall velocities and peak temperatures in the environment of massive haloes contribute to the differential evolution of bright and faint LAEs. The relative contribution of the evolution of peculiar/infall velocities and the spatial correlations with ionized regions on the visibility of LAEs thereby depends strongly on the assumed reionization history.

(iii) It is the faint emitters that more closely trace the evolution of the volume-filling fraction of ionized regions, since the gas in their local environments is not rapidly evolving (as it is for the bright emitters). We thus recommend that studies of the reionization history continue to focus on the fainter LAEs.

(iv) In our simulations, the infalling gas in the outskirts of the halo (just outside the virial radius) has a strong effect on the visibility of the LAE it is hosting. This is in agreement with the suggestion by Sadoun et al. (2017) that before percolation the infalling gas in the outskirts of LAE host haloes in already ionized regions is still sufficiently neutral to cause a rapid evolution of LAE visibility at $6 < z < 7$. In our simulations, the photoionization rate in ionized regions is higher than was modelled in that work, but the self-shielding is still sufficient to strongly attenuate the Ly α emission from the galaxy. In particular, we find that this effect is stronger in the more massive haloes. This means that for observations of UV bright galaxies living in such massive hosts, deriving constraints on the volume-filling neutral fraction of the IGM involves more complicated modelling of such self-shielding than for UV faint LAEs living in less massive haloes. This reinforces our recommendation that future observational studies focus on UV faint LAEs for constraining reionization. Alternatively, selecting LAEs based on intrinsic velocity offset could sample those galaxies whose emission is least attenuated by the self-shielded gas of the CGM.

(v) Overall, our updated modelling with the higher dynamic range Sherwood simulation gives similar results to CPBH15, albeit with some notable differences:

(a) We confirm that the 'Late' and 'Very Late' reionization histories favoured in CPBH15, which also match Ly α forest data, are a good match to the observed rapid evolution of faint Ly α emitters. Note, however, that unlike CPBH15, we can obtain this agreement without invoking an evolution of the redshift of the intrinsic Ly α emission relative to systemic. This is possibly due to the more consistent treatment of peculiar velocities in our simulations made possible by dropping the hybrid approach of CPBH15 (who combined a rather small box-size hydrodynamical simulation with a large box-size dark matter simulation). We further confirm that the evolution of the ionizing emissivity in the popular HM12 UV background model corresponds to a decrease of the volume factor of ionized regions at $z > 6$ that is too slow to explain the rapid disappearance of faint LAEs.

(b) As in CPBH15, in our updated simulations the rapid decrease of the visibility of faint Ly α emitters is mainly due to the rapid evolution of the volume-filling fraction of ionized regions in our models. In our fiducial updated model, we have used the self-shielding prescription suggested by Chardin et al. (2018), who have explicitly modelled the self-shielding in ionized regions before the full percolation of ionized regions with full radiative transfer simulations. Note, in particular, that with this prescription, the effect of self-shielding is significantly weaker than with the widely used Rahmati et al. (2013) model. If self-shielding is indeed as weak as suggested by the Chardin et al. (2018) simulations, then reproducing the rapid evolution of faint Ly α emitters at $z > 6$ may require a reionization history where reionization occurs as late as in our 'Very Late' model.

The rapid disappearance of faint Ly α emitters arguably provides the strongest constraints to date on the reionization history of hydrogen at $z > 6$, and our simulations confirm that their rapid disappearance is a strong evidence for a rather late reionization.

ACKNOWLEDGEMENTS

We would like to thank Renske Smit and George Efstathiou for constructive comments, and Kazuaki Ota for useful discussion. We also thank an anonymous referee for helpful comments. LHW is supported by the Science and Technology Facilities Council (STFC). Support by ERC Advanced Grant 320596 'The Emergence of Structure During the Epoch of Reionization' is gratefully acknowledged. We acknowledge PRACE for awarding us access to the Curie supercomputer, based in France at the Trés Grand Centre de Calcul (TGCC). This work used the DiRAC Data Centric system at Durham University, operated by the Institute for Computational Cosmology on behalf of the STFC DiRAC HPC Facility (www.dirac.ac.uk). This equipment was funded by BIS National E-infrastructure capital grant ST/K00042X/1, STFC capital grants ST/H008519/1, and ST/K00087X/1, STFC DiRAC Operations grant ST/K003267/1 and Durham University. DiRAC is part of the National E-Infrastructure. This work made use of the `SciPy` (Jones et al. 2001) ecosystem of libraries for Python including: `NumPy` (van der Walt, Colbert & Varoquaux 2011), `Matplotlib` (Hunter 2007), and `Cython` (Behnel et al. 2011).

REFERENCES

Aubert D., Teyssier R., 2008, MNRAS, 387, 295
Barkana R., 2004, MNRAS, 347, 59
Barnes L. A., Haehnelt M. G., Tescari E., Viel M., 2011, MNRAS, 416, 1723
Becker G. D., Bolton J. S., 2013, MNRAS, 436, 1023
Becker G. D., Bolton J. S., Haehnelt M. G., Sargent W. L. W., 2011, MNRAS, 410, 1096
Becker G. D., Bolton J. S., Madau P., Pettini M., Ryan-Weber E. V., Venemans B. P., 2015, MNRAS, 447, 3402
Behnel S., Bradshaw R., Citro C., Dalcin L., Seljebotn D. S., Smith K., 2011, Comput. Sci. Eng., 13, 31
Bolton J. S., Haehnelt M. G., 2007, MNRAS, 374, 493
Bolton J. S., Haehnelt M. G., 2013, MNRAS, 429, 1695
Bolton J. S., Puchwein E., Sijacki D., Haehnelt M. G., Kim T.-S., Meiksin A., Regan J. A., Viel M., 2017, MNRAS, 464, 897
Bond J. R., Cole S., Efstathiou G., Kaiser N., 1991, ApJ, 379, 440
Bouwens R. J. et al., 2015, ApJ, 803, 34
Calverley A. P., Becker G. D., Haehnelt M. G., Bolton J. S., 2011, MNRAS, 412, 2543
Chardin J., Haehnelt M. G., Aubert D., Puchwein E., 2015, MNRAS, 453, 2943
Chardin J., Kulkarni G., Haehnelt M. G., 2018, MNRAS, 478, 1065
Charlot S., Fall S. M., 1993, ApJ, 415, 580
Choudhury T. R., 2009, Curr. Sci., 97, 841
Choudhury T. R., Haehnelt M. G., Regan J., 2009, MNRAS, 394, 960
Choudhury T. R., Puchwein E., Haehnelt M. G., Bolton J. S., 2015, MNRAS, 452, 261
Curtis-Lake E. et al., 2012, MNRAS, 422, 1425
Dayal P., Ferrara A., 2012, MNRAS, 421, 2568
Dayal P., Ferrara A., Saro A., Salvaterra R., Borgani S., Tornatore L., 2009, MNRAS, 400, 2000
Dijkstra M., 2014, PASA, 31, e040
Dijkstra M., Haiman Z., Spaans M., 2006, ApJ, 649, 14
Dijkstra M., Lidz A., Wyithe J. S. B., 2007, MNRAS, 377, 1175
Dijkstra M., Mesinger A., Wyithe J. S. B., 2011, MNRAS, 414, 2139
Draine B. T., 2011, Physics of the Interstellar and Intergalactic Medium. Princeton University Press, Princeton, New Jersey
Duncan K., Conselice C. J., 2015, MNRAS, 451, 2030
Erb D. K., Pettini M., Shapley A. E., Steidel C. C., Law D. R., Reddy N. A., 2010, ApJ, 719, 1168
Erb D. K. et al., 2014, ApJ, 795, 33
Fan X. et al., 2006, AJ, 132, 117
Faucher-Giguère C.-A., Lidz A., Zaldarriaga M., Hernquist L., 2009, ApJ, 703, 1416
Finkelstein S. L. et al., 2015, ApJ, 810, 71
Finlator K., Oppenheimer B. D., Davé R., 2011, MNRAS, 410, 1703
Finlator K. et al., 2017, MNRAS, 464, 1633
Furlanetto S. R., Zaldarriaga M., Hernquist L., 2004, ApJ, 613, 1

Furlanetto S. R., Schaye J., Springel V., Hernquist L., 2005, ApJ, 622, 7
Greig B., Mesinger A., 2017, MNRAS, 465, 4838
Gronke M., Dijkstra M., 2016, ApJ, 826, 14
Gronke M., Bull P., Dijkstra M., 2015, ApJ, 812, 123
Haardt F., Madau P., 2012, ApJ, 746, 125
Hassan S., Davé R., Finlator K., Santos M. G., 2016, MNRAS, 457, 1550
Hu E. M., Cowie L. L., McMahon R. G., 1998, ApJ, 502, L99
Hu E. M., Cowie L. L., Barger A. J., Capak P., Kakazu Y., Trouille L., 2010, ApJ, 725, 394
Hunter J. D., 2007, Comput. Sci. Eng., 9, 90
Inoue A. K. et al., 2018, PASJ, 70, 50
Itoh R. et al., 2018, preprint (arXiv:1805.05944)
Jones E. et al., 2001, SciPy: Open source scientific tools for Python, http://www.scipy.org/
Kaiser N., 1984, ApJ, 284, L9
Kakiichi K., Dijkstra M., Ciardi B., Graziani L., 2016, MNRAS, 463, 4019
Kashikawa N. et al., 2006, ApJ, 648, 7
Konno A. et al., 2014, ApJ, 797, 16
Konno A. et al., 2018, PASJ, 70, S16
Kuhlen M., Faucher-Giguère C.-A., 2012, MNRAS, 423, 862
Kulkarni G., Choudhury T. R., Puchwein E., Haehnelt M. G., 2016, MNRAS, 463, 2583
Kulkarni G., Choudhury T. R., Puchwein E., Haehnelt M. G., 2017, MNRAS, 469, 4283
Majumdar S., Mellema G., Datta K. K., Jensen H., Choudhury T. R., Bharadwaj S., Friedrich M. M., 2014, MNRAS, 443, 2843
Mason C. A., Trenti M., Treu T., 2015, ApJ, 813, 21
Mason C. A. et al., 2018, ApJ, 857, L11
Matthee J., Sobral D., Santos S., Röttgering H., Darvish B., Mobasher B., 2015, MNRAS, 451, 400
McGreer I. D., Mesinger A., D'Odorico V., 2015, MNRAS, 447, 499
McGreer I. D., Fan X., Jiang L., Cai Z., 2018, AJ, 155, 131
Meiksin A. A., 2009, Rev. Mod. Phys., 81, 1405
Mesinger A., Furlanetto S., 2007, Astrophys. J., 669, 663
Mesinger A., Furlanetto S., Cen R., 2011, MNRAS, 411, 955
Mesinger A., Aykutalp A., Vanzella E., Pentericci L., Ferrara A., Dijkstra M., 2015, MNRAS, 446, 566
Mo H., van den Bosch F. C., White S., 2010, Galaxy Formation and Evolution., Cambridge University Press, Cambridge
Ono Y. et al., 2012, ApJ, 744, 83
Orsi A., Lacey C. G., Baugh C. M., 2012, MNRAS, 425, 87
Ota K. et al., 2017, ApJ, 844, 85
Ouchi M. et al., 2008, ApJS, 176, 301
Ouchi M. et al., 2010, ApJ, 723, 869
Ouchi M. et al., 2018, PASJ, 70, S13
Partridge R. B., Peebles P. J. E., 1967, ApJ, 147, 868
Pentericci L. et al., 2014, ApJ, 793, 113
Planck Collaboration XVI, 2014, A&A, 571, A16
Planck Collaboration XLVII, 2016, A&A, 596, A108
Puchwein E., Haardt F., Haehnelt M. G., Madau P., 2018, preprint (arXiv:1801.04931)
Rahmati A., Pawlik A. H., Raičevic M., Schaye J., 2013, MNRAS, 430, 2427
Richards G. T. et al., 2006, AJ, 131, 2766
Robertson B. E. et al., 2013, ApJ, 768, 71
Rybicki G. B., Lightman A. P., 1985, Radiative Processes in Astrophysics. John Wiley & Sons, New York
Sadoun R., Zheng Z., Miralda-Escudé J., 2017, ApJ, 839, 44
Santos M. R., 2004, MNRAS, 349, 1137
Santos M. G., Ferramacho L., Silva M. B., Amblard A., Cooray A., 2010, MNRAS, 406, 2421
Santos S., Sobral D., Matthee J., 2016, MNRAS, 463, 1678
Schaye J., 2001, ApJ, 559, 507
Schenker M. A., Stark D. P., Ellis R. S., Robertson B. E., Dunlop J. S., McLure R. J., Kneib J.-P., Richard J., 2012, ApJ, 744, 179
Shapley A. E., Steidel C. C., Pettini M., Adelberger K. L., 2003, ApJ, 588, 65
Shibuya T. et al., 2014, ApJ, 788, 74
Silva M. B., Kooistra R., Zaroubi S., 2016, MNRAS, 462, 1961
Sobacchi E., Mesinger A., 2015, MNRAS, 453, 1843
Springel V., 2005, Mon. Notices R. Astron. Soc., 364, 1105
Springel V., Yoshida N., White S. D. M., 2001, New A, 6, 79
Stark D. P., Ellis R. S., Chiu K., Ouchi M., Bunker A., 2010, MNRAS, 408, 1628
Stark D. P., Ellis R. S., Ouchi M., 2011, ApJ, 728, L2
Stark D. P. et al., 2015, MNRAS, 450, 1846
Stark D. P. et al., 2017, MNRAS, 464, 469
Steidel C. C., Erb D. K., Shapley A. E., Pettini M., Reddy N., Bogosavljević M., Rudie G. C., Rakic O., 2010, ApJ, 717, 289
Tepper-García T., 2006, MNRAS, 369, 2025
Trenti M., Stiavelli M., Bouwens R. J., Oesch P., Shull J. M., Illingworth G. D., Bradley L. D., Carollo C. M., 2010, ApJ, 714, L202
Treu T., Trenti M., Stiavelli M., Auger M. W., Bradley L. D., 2012, ApJ, 747, 27
van der Walt S., Colbert S. C., Varoquaux G., 2011, Comput. Sci. Eng., 13, 22
Verde L. et al., 2002, MNRAS, 335, 432
Viel M., Haehnelt M. G., Springel V., 2004, MNRAS, 354, 684
Willott C. J., Carilli C. L., Wagg J., Wang R., 2015, ApJ, 807, 180
Worseck G. et al., 2014, MNRAS, 445, 1745
Wyithe J. S. B., Bolton J. S., 2011, MNRAS, 412, 1926
Yang H., Malhotra S., Gronke M., Rhoads J. E., Dijkstra M., Jaskot A., Zheng Z., Wang J., 2016, ApJ, 820, 130
Yue B., Ferrara A., Xu Y., 2016, MNRAS, 463, 1968
Zahn O., Lidz A., McQuinn M., Dutta S., Hernquist L., Zaldarriaga M., Furlanetto S. R., 2007, ApJ, 654, 12
Zheng Z., Cen R., Trac H., Miralda-Escudé J., 2010, ApJ, 716, 574
Zheng Z.-Y. et al., 2017, ApJ, 842, L22
Zitrin A. et al., 2015, ApJ, 810, L12

APPENDIX A: ANALYTIC MODELLING OF HALO INFALL PROFILES

In this appendix, we discuss an analytical method for calculating the infall velocity profile around collapsed haloes. This is then applied to find the velocity profiles we might expect to see around the average mass haloes of our different mass models. We can then compare these profiles with the median profiles in our simulation, as shown in Fig. 5. Finally, we construct a simplistic model for the IGM gas surrounding an LAE using these analytic velocity profiles; we then use this to calculate the difference in transmission due to a differential velocity evolution. This differential transmission evolution is similar to that found in the simulations as described in Section 6.

Our calculation closely follows that of Barkana (2004) and Sadoun et al. (2017); nevertheless, we summarize the main steps for completeness. The analytical calculation consists of two parts:

(i) calculation of the linearly extrapolated initial density profile around the halo using the excursion set formalism;
(ii) solving the non-linear problem for overdense spherical shells around the halo using the standard spherical collapse formalism.

A1 Linearly extrapolated density profile

Let us consider a halo of mass M formed at some redshift z. In the language of excursion sets, this problem can be mapped into a random walk problem in the $s - \delta$ plane, where s is the variance of the linearly extrapolated density contrast smoothed over some Lagrangian scale r and δ is the linearly extrapolated smoothed density contrast at the same scale. Note that s, r, and the corresponding

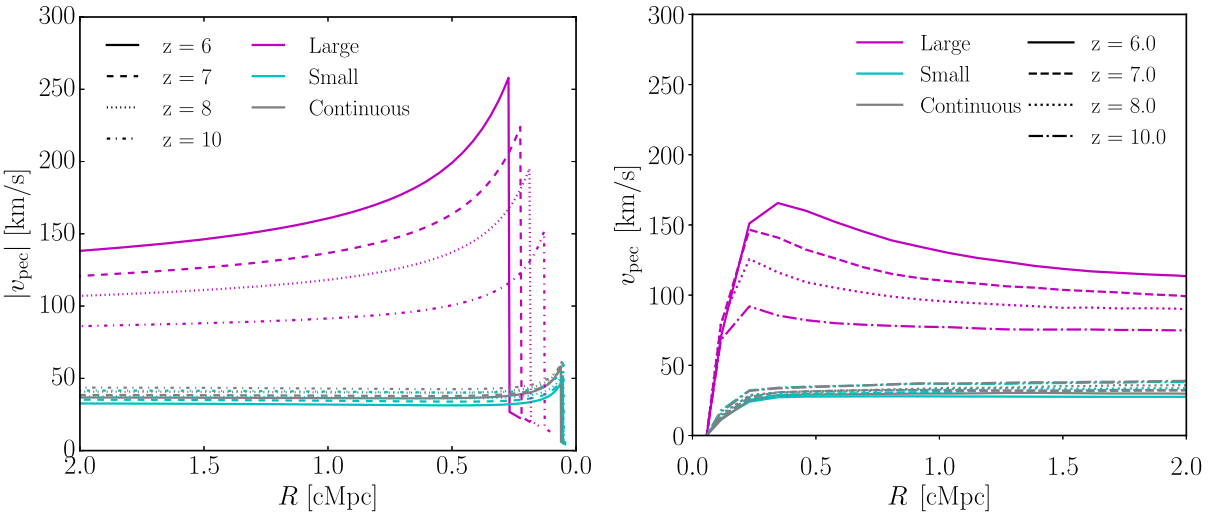

Figure A1. Absolute values for the sightline peculiar velocity of gas surrounding the halo. *Left-hand panel*: Analytic predictions for the infalling velocity. *Right-hand panel*: Median velocity profiles from the simulation (where the median is taken from the appropriately orientated sample of infall velocities, and then the absolute value is taken). Note that the abscissa has been mirrored about the vertical line between the panels to aid comparison.

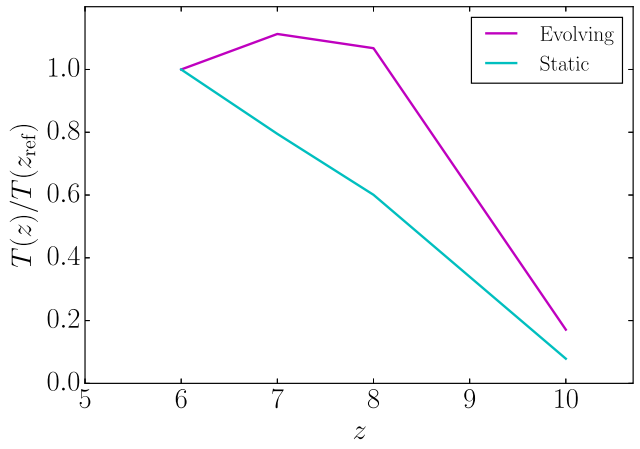

Figure A2. Mean transmission fraction evolution for the analytic models: 'evolving' and 'static' with peculiar velocity structures based on the large and small-mass models as shown in Fig. A1. With only a difference in velocity structure, the mean transmission fraction evolution is changed dramatically, causing the 'evolving' model LAEs to be more visible out to higher redshifts than the 'static' LAEs.

mass scale m are related by the relations,

$$s = \int_0^\infty \frac{{\rm d}k}{k} \frac{k^3 P(k)}{2\pi^2} W^2(kr), m = \frac{4\pi}{3} \bar{\rho} r^3, \tag{A1}$$

where $P(k)$ is the matter power spectrum linearly extrapolated to $z = 0$, $\bar{\rho}$ is the present mean matter density of the universe, and $W(kr)$ is the smoothing filter in Fourier space.

The formation of a halo corresponds to the first upcrossing of $\delta(s)$ of a threshold or a 'barrier', $\delta_{\rm c}(z)$, by random walks in the $s - \delta$ plane. In the spherical approximation, the barrier is independent of the scale s and is given by $\delta_{\rm c}(z) = 1.686/D(z)$, $D(z)$ being the linear growth factor. The scale at which this upcrossing happens can be denoted by s_M which typically falls near the variance corresponding to the mass M. The linearly extrapolated density profile outside the halo can then be obtained from the distribution of $\delta(s)$ for $s \leq s_M$, with the condition that the random walks first upcross the barrier at s_M. It can be shown that the probability distribution of the linearly extrapolated density profile can be written as

$$P(\delta, s|s_M) = \frac{f(s_M|\delta, s)}{f(s_M)} Q(\delta, s), \tag{A2}$$

where $f(s_M)$ is the first upcrossing distribution, $f(s_M|\delta, s)$ is the *conditional* first upcrossing distribution, and $Q(\delta, s)$ is the probability that the walk has height δ at s and remained below the barrier at all $s < s_M$.

In the case where the smoothing filter is chosen to be a tophat in k-space (i.e. the sharp-k filter), the steps of the random walks become uncorrelated. In that case, we can write the above quantities as

$$\begin{aligned} f(s_M) &= \frac{1}{\sqrt{2\pi}} \frac{\delta_{\rm c}(z)}{s_M^{3/2}} \exp\left(-\frac{\delta_{\rm c}^2(z)}{2s_M}\right), \\ f(s_M|\delta, s) &= \frac{1}{\sqrt{2\pi}} \frac{\delta_{\rm c}(z) - \delta}{(s_M - s)^{3/2}} \exp\left(-\frac{[\delta_{\rm c}(z) - \delta]^2}{2(s_M - s)}\right), \\ Q(\delta, s) &= \frac{1}{\sqrt{2\pi s}} \left[\exp\left(-\frac{\delta^2}{2s}\right) \right. \\ &\quad \left. - \exp\left(-\frac{(2\delta_{\rm c}(z) - \delta)^2}{2s}\right)\right]. \end{aligned} \tag{A3}$$

The mean density profile is simply given by

$$\langle \delta(s) \rangle_M \equiv \int_{-\infty}^{\delta_{\rm c}(z)} {\rm d}\delta \delta P(\delta, s|s_M), \tag{A4}$$

where s_M is set to the variance corresponding to mass M. This equation has the closed form solution (Barkana 2004),

$$\begin{aligned} \frac{\langle \delta(s) \rangle_M}{\delta_{\rm c}(z)} &= 1 - \left(1 - \alpha + \frac{\alpha}{\beta}\right) {\rm erf}\left(\sqrt{\frac{\beta(1-\alpha)}{2\alpha}}\right) \\ &\quad - \sqrt{\frac{2\alpha(1-\alpha)}{\pi\beta}} \exp\left(-\frac{\beta(1-\alpha)}{2\alpha}\right), \end{aligned} \tag{A5}$$

where

$$\alpha \equiv \frac{s}{s_M}, \beta \equiv \frac{\delta_{\rm c}^2(z)}{s_M}. \tag{A6}$$

Note that the calculation above assumes a sharp-k filter for the random walks but a real-space tophat filter for calculating the barrier

height $\delta_c(z)$ (Bond et al. 1991). Removal of this inconsistency requires self-consistent usage of the real-space tophat filter for studying the random walks. However, this leads to steps that are correlated and are generally difficult to deal with. Barkana (2004) proposed an ansatz based on the limit when the halo corresponds to a rare peak $\beta \to \infty$. In that case, one can replace the two parameters α and β by the following

$$\alpha \equiv \frac{\xi(r_M, r)}{s_M}, \beta \equiv \frac{\delta_c^2(z)\alpha(1-\alpha)}{s - \alpha\xi(r_M, r)}, \tag{A7}$$

where $r(r_M)$ is the Lagrangian length-scale corresponding to $s(s_M)$, and

$$\xi(r_M, r) = \int_0^\infty \frac{\mathrm{d}k}{k} \frac{k^3 P(k)}{2\pi^2} W(kr_M)W(kr). \tag{A8}$$

The quantity $W(x)$ is the k-space function corresponding to a spherical tophat window in position space. We follow the above ansatz in our work as well.

A2 Spherical collapse

Now, consider the Lagrangian scale r with mass m and linearly extrapolated density contrast $\delta = \langle \delta(s) \rangle_M$. If we assume that the matter in a region enclosed by r evolves under spherical symmetry, we can apply the solutions of the spherical collapse directly. Since we are concerned with rather high redshifts $z \gtrsim 6$, we can work with the analytical solutions obtained for the standard Einstein–deSitter universe.

The evolution of the spherical shell with linearly extrapolated density contrast δ and enclosed mass m is given by the parametric solution (see, for example, Mo, van den Bosch & White 2010, Section 5.1.1)

$$R = A\,(1 - \cos\theta), \quad t = B(\theta - \sin\theta),$$
$$B = \frac{6t_i}{(20\,\delta_i/3)^{3/2}}, \quad A^3 = GmB^2, \tag{A9}$$

where t_i is the initial time and $\delta_i = D(t_i)\delta$. Note that the radius R in the above solution is in proper units. The velocity of the shell is then

$$v = \frac{A}{B}\frac{\sin\theta}{1 - \cos\theta}. \tag{A10}$$

The peculiar velocity is obtained by subtracting the Hubble velocity $H(t)\,R$ from the above, i.e.

$$v_{\rm pec} = v - H(t)\,R. \tag{A11}$$

Note that $v_{\rm pec} > 0$ for outflowing or expanding matter. Since we are interested in the infall velocity around the haloes, we shall plot the magnitude of the velocity, $|v_{\rm pec}|$, to compare between the analytic model and the simulations.

The above solution breaks down once tangential motions and shell crossings become important. In that case, the collisionless dark matter virializes via violent relaxation while the baryons undergo various non-linear processes that lead to the formation of galaxies. Since such non-linear processes are difficult to account for, usually one assumes that the time of virialization (or collapse) is that corresponding to $\theta = 2\pi$, and the final virial radius is given by the virial energy condition that turns out to be

$$R_{\rm vir} = A. \tag{A12}$$

According to solution (A9), the value of R approaches $R_{\rm vir}$ when $\theta = 3\pi/2$. Clearly, the spherically symmetric solution has crossed the regime of validity by then. We make the simplifying assumption that the radius remains constant for $\theta > 3\pi/2$

$$R = \begin{cases} A(1 - \cos\theta) & \text{when } \theta \le \dfrac{3\pi}{2}, \\ A & \text{otherwise.} \end{cases} \tag{A13}$$

Correspondingly, the radial velocity is assumed to be

$$v = \begin{cases} \dfrac{A}{B}\dfrac{\sin\theta}{1 - \cos\theta} & \text{when } \theta \le \dfrac{3\pi}{2}, \\ 0 & \text{otherwise.} \end{cases} \tag{A14}$$

The above relation assumes that as the halo approaches virialization, the radial velocity becomes zero and all the kinetic energy has been converted into random motions.

The two equations (A13) and (A14) together give the velocity profile that can be directly compared with simulation results. The calculation is strictly meant for collisionless matter; however, we apply it to the gas profile under the assumption that the gas follows the dark matter outside the virial radius (as in Sadoun et al. 2017).

A3 Comparison with simulation velocity profiles

We apply this formalism to calculate the velocity profiles for masses corresponding to the average masses of our models. These masses are shown for $z = 6$, 7, 8, and 10 in Table 1. The resulting profiles for the large, small, and continuous average mass haloes can be seen in Fig. A1.

In Fig. A1, we see the same behaviour observed in the median profiles from the simulation. In particular, we see a similar redshift evolution of the profiles across the models: in the large model, we see an increase in infall velocities with decreasing redshift; conversely in the small and continuous models, we see a much smaller evolution (and in the opposite direction – peak velocity increasing with redshift). This effect plays a role in the different evolution of the visibility of the models, as discussed in Section 6.

A4 The effect of infall velocity evolution

In order to test whether this infalling velocity evolution can lead to a differential visibility evolution, we construct two simple models for the gas properties around the host halo of an LAE. We keep the neutral hydrogen density, $n_{\rm HI}$, and gas temperature, $T_{\rm HI}$, the same in both models; we then use the velocity profiles calculated with equation (A14) (seen in Fig. A1) to construct an 'evolving' velocity profile and a 'static' profile. The 'evolving' profile has a larger infalling velocity amplitude, as well as a strong evolution with redshift, and it therefore presents a similar gas environment to that around the large-mass model haloes. In comparison for the 'static' profile, we fixed the velocity profile to be constant with redshift, and with a lower infalling amplitude, as is the case for the environments around the small-mass model haloes.

In order to create a similar macroscopic evolution of the Ly α transmission as we see in the simulations, we set the neutral hydrogen fraction around the LAE to be either an equilibrium value $x_{\rm HI} = x_{\rm eq}$ (found using $\Gamma_{\rm HI}$) or $x_{\rm HI} = 1$ (for regions not yet reionized), based on $Q_{\rm M}$. We use $Q_{\rm M}$ and $\Gamma_{\rm HI}$ from the Late reionization history. The temperature of the gas is fixed at $T_{\rm HI} = 10^4$ K, and the total hydrogen density is chosen to be the mean cosmic hydrogen density. This crude modelling of $n_{\rm HI}$ and $T_{\rm HI}$ is intended as a zeroth-order description the IGM gas and importantly is the same for each case

('evolving' or 'static'). Given these gas properties, we calculate the Ly α transmission as in Section 3.

The resulting mean transmission fraction (TFR) evolution is shown in Fig. A2 for the 'evolving' profile in magenta and the 'static' model in cyan. We see that the 'evolving' profile results in a slower evolution of the transmission.

We note that the presence of this infalling gas velocity evolution can therefore lead to a differential visibility in LAEs. The magnitude of this difference in the visibility is dependent on the neutral gas density; in reality, the profiles close to the host halo will differ significantly from the crude model discussed above.

This effect can be understood as follows: when the infalling velocities are comparable to the intrinsic offset of the emission, then neutral gas close to the emitter will strongly absorb Ly α. As these velocities decrease with increasing redshift, there will be a decrease in the absorption from this self-shielded CGM gas. This decrease in absorption acts counter to the increase in absorption in the neutral gas of the larger scale IGM, which is increasing with redshift (as less reionization has occurred). Hence, this velocity structure can counter some of the transmission evolution and will – despite itself being due to a *rapid* evolution of the velocity amplitude – *slow* the transmission evolution in the more massive haloes where it can be significant.

APPENDIX B: FURTHER MODEL VARIATIONS

We have also explored further variations to the nine model combinations presented in this work. In particular, we vary the emission profile model from our fiducial by considering different intrinsic velocity offsets.

The default model in this work assumed a Gaussian emission profile, with width $\sigma_v = 88\,\mathrm{km\,s^{-1}}$ and line-centre offset from Ly α by $\Delta v_{\rm int} = 100\,\mathrm{km\,s^{-1}}$. This model tries to account for the complex radiative transfer within the galaxy that leads to a reddened peak. We applied this model to all haloes, regardless of mass.

We now test a second model using a bimodal distribution of profiles: for the small-mass range, we use the default $\Delta v_{\rm int} = 100\,\mathrm{km\,s^{-1}}$, but for the large-mass range, we use a larger offset of $\Delta v_{\rm int} = 300\,\mathrm{km\,s^{-1}}$. This bimodal model is motivated by some recent observational results, for example, Willott et al. (2015) and Stark et al. (2017), which have found that the most luminous LAEs at $z \sim 6$ can have $\Delta v_{\rm int} = 300$ – $500\,\mathrm{km\,s^{-1}}$. We also test a third model, which varies the velocity offset as a function of redshift,

$$\Delta v_{\rm int} = 100 \left(\frac{1+z}{7}\right)^{-3} \mathrm{km\,s^{-1}}. \quad \text{(B1)}$$

This model was employed in CPBH15 to explore further enhancements to the IGM absorption and was found to aid the agreement with the data.

In the left-hand panel of Fig. B1, we show the TFR evolution for the large-mass and small-mass models using the mass-dependent profile. The evolution of the large model is changed slightly but not dramatically. Although this bimodal profile can lead to much higher transmission fractions in the large-mass model, it does so for all redshifts, and hence the TFRs (which are ratios across redshifts) are broadly unaffected. We note, however, that the scatter in the TFR is greatly reduced compared to the fixed emission profile TFRs.

In the right-hand panel of Fig. B1, we show the TFR evolution for the continuous model with the redshift-dependent emission profile. Here we see an increase in attenuation that increases the agreement between the data and the 'Late' reionization history. If indeed the velocity offset of LAEs evolves in such a manner, this would reinforce the conclusion that reionization progressed in a 'Late' history.

We therefore find that our main conclusions regarding the differential evolution of different mass LAE host haloes and the best-fitting reionization history are robust to these changes in emission profile.

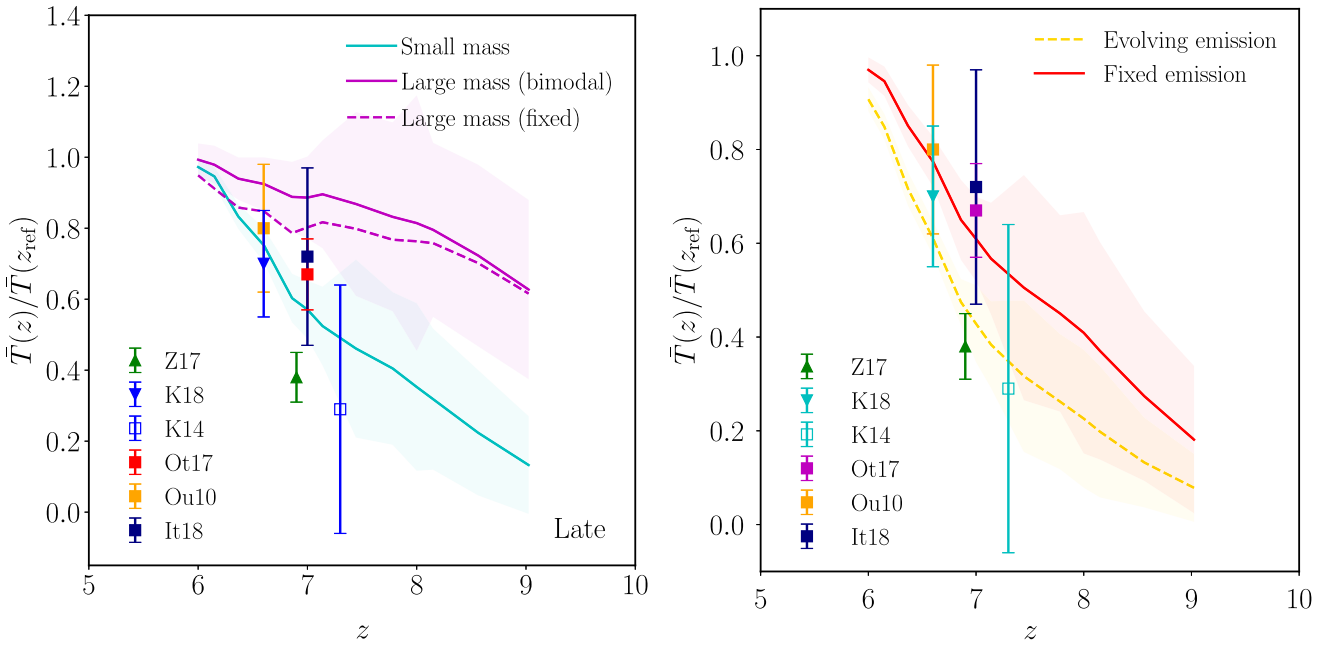

Figure B1. *Left-hand panel*: The TFR evolution for the large- and small-mass models, using the mass-dependent 'bimodal' emission profile. For comparison, the default emission profile ('fixed') is shown as a dashed line. Overplotted are observed TFR values, as in Fig. 8. *Right-hand panel*: TFR evolution in the continuous model with the Late reionization history: comparing a redshift-dependent emission profile to the default fixed profile. The evolving velocity offset leads to an increased Ly α attenuation.

This paper has been typeset from a TEX/LATEX file prepared by the author.